Disruption of orbitofrontal-hypothalamic projections in a murine ALS model and human patients

Authors: David Bayer[1,2], Stefano Antonucci[1], Hans-Peter Müller[1], Luc Dupuis[3], Tobias M. Boeckers[4,5], Albert C. Ludolph[1,5], Jan Kassubek[1], Francesco Roselli[1,5]

E-Mail: david.bayer@uni-ulm.de, stefano.antonucci@uni-ulm.de, hans-peter.mueller@uni-ulm.de, ldupuis@neuro-cnrs.unistra.fr, tobias.boeckers@uni-ulm.de, albert.ludolph@rku.de, jan.kassubek@uni-ulm.de, francesco.roselli@uni-ulm.de

Affiliation:

1. Dept. of Neurology, Ulm University, Ulm DE
2. CEMMA (Cellular and Molecular Mechanisms in Aging) research training group, Ulm DE
3. University of Strasbourg
4. Institute of Anatomy and Cell Biology, Ulm University, Ulm DE
5. German Center for Neurodegenerative Diseases-DZNE, Ulm DE

Corresponding authors: Francesco Roselli,
Center for Biomedical Research (ZBF)
Helmholtzstrasse 8-89081 Ulm (DE)
Phone: 0049-0731-500-63147
Email: francesco.roselli@uni-ulm.de

Abstract

Increased catabolism is a new clinical manifestation of Amyotrophic Lateral Sclerosis. A dysfunction of lateral hypothalamus may drive hypermetabolism in ALS; however, Its causes and anatomical substrates are unknown. We hypothesize that disruption cortico-hypothalamic circuits may impair energy homeostasis in ALS. We used rAAV2 for large-scale projection mapping and image analysis pipeline based on Wholebrain and Ilastik to quantify projections from the forebrain to the latera hypothalamus of the SOD1(G93A) ALS mouse model as well as of the $Fus^{\Delta NLS}$ ALS mouse model. Expanded projections from agranular Insula, ventrolateral orbitofrontal and secondary motor cortex to lateral hypothalamus were found in two independent cohorts of the hypermetabolic SOD1(G93A) ALS model. The non-hypermetabolic $Fus^{\Delta NLS}$ ALS mouse model display a loss of projections from motor cortex but no change in projections from insula and orbitofronal cortex. 3T DTI-MRI data on 83 ALS patients and 65 controls confirmed the disruption of the orbitofrontal-hypothalamic tract in ALS patients. Converging murine and human data demonstrate the selective disruption of hypothalamic inputs in ALS as a factor contributing to the origin of hypermetabolism.

Key words: rAAV2; Agranular Insula; Orbitofrontal Cortex; Lateral Hypothalamus; Hypermetabolism; Amyotrophic lateral sclerosis

Introduction

Amyotrophic lateral sclerosis (ALS) is traditionally conceptualized as a neurodegenerative condition primarily affecting upper motoneurons, located in primary motor cortex, and lower motoneurons, located in spinal cord, whose dysfunction and loss determines a relentless, progressive and ultimately fatal motor impairment [1]. More recently, hypermetabolism has been recognized as an additional, non-motor clinical feature of ALS [2]. Epidemiological surveys have revealed that ALS patients display increased catabolism [2, 3] and pointed out lower body-mass index constitutes a risk factor for ALS [4]. Furthermore, reduced levels of metabolic rate proxies such as plasma lipids and body fat content are predictors of survival of ALS patients [5-7], i.e. weight loss is strongly correlated with shorter survival [8]. Increased catabolism appears to be due to intrinsic hypermetabolism both in ALS patients [9-13] as well as in mutant SOD1 ALS mice [14]. Notably, metabolism and energy balance actually constitute promising targets for intervention, since increasing caloric intake has beneficial effects on survival, particularly on fast-progressing ALS patients [15].

Mechanistic insights into ALS hypermetabolism remain limited. Hypothalamic nuclei receive and integrate inputs coming from a large fraction of the brain [16-19] in order to establish the proper balance of feeding, energy storage and energy expenditure [20]. Thus, disruption of these inputs may be sufficient to drive metabolic imbalances. In fact, the overall architecture between large-scale networks appear to be disturbed in ALS [21-25] and ALS-related pathobiochemistry affects a significant proportion of cortical and subcortical structures, in a pattern evolving with disease progression [26, 27]. We have hypothesized that a similar degree of disruption and remodeling may take place in large-scale networks providing inputs to the

66 feeding-regulating Lateral Hypothalamic Area (LHA) and that such a disruption may coincide
67 with the appearance of the hypermetabolic phenotype. We have now identified the selective
68 disruption of projections from insular and orbitofrontal cortex to LHA in ALS mouse model as
69 well as in human ALS patients by a combination of retrograde rAAV-2 tracing and MRI-DTI tract
70 tracing.
71
72 **Methods**
73
74 *Animals*
75 All experimental procedures involving animals were performed in agreement with the
76 guidelines for the welfare of experimental animals issued by the Federal Government of
77 Germany; all experiments were approved by the Regierungspräsidium Tübingen under the
78 animal license- number 1390 and by the Ulm University Tierforschungszentrum committee. No
79 effort was spared to implement "3R" guidelines for animal experimentation.
80 We obtained from Jackson Laboratories the following strains: B6SJL73 Tg(SOD1*G93A)1Gur/J
81 (high-copy), (henceforth mSOD) and B6.Cg-Gt(ROSA)26Sor$^{tm6/(CAG74ZsGreen)Hze/J}$ (henceforth
82 ZsGreen). To generate the mSOD/ZsGreen double transgenic mice, hemizygous mSOD males
83 were crossed with homozygous ZsGreen$^{+/+}$ females as previously reported [21]; the progeny
84 included mSOD^{+}/ZsGreen$^{+/-}$ mice at the expected mendelian rate. mSOD^{+}/ZsGreen$^{+/-}$ are
85 henceforth going to be labelled mSOD1 and mSOD^{-}/ZsGreen$^{+/-}$will be labelled WT.
86 The heterozygous B6.Fus$^{\Delta NLS/+}$ (henceforth Fus) were provided by Luc Dupuis from the Faculté
87 de Médecine, Strasbourg, France [28]. For the generation of Fus/ZsGreen double transgenic

88 mice, heterozygous Fus males were crossed with homozygous ZsGreen$^{+/+}$ females. The progeny
89 included Fus^{-}/ZsGreen$^{+/-}$ mice at the expected mendelian rate. Fus^{-}/ZsGreen$^{+/-}$ are henceforth
90 going to be labelled kiFUS.
91
92 Mice were housed at 2 - 5 animals per cage, with unlimited access to food and water, a
93 light/dark cycle of 12/12 hr and humidity between 40% and 60%. All mice expressing mSOD
94 were routinely tested for motor impairment and euthanized in case of overt motor disability.
95 Since male and female mice have differ substantially in progression rates of clinical and
96 biological manifestation of motoneuron disease (e.g. [29]), the present study focused on male
97 mice only.
98
99 *Viral vectors*
100 Retrograde rAAV2 [30] vectors encoding for the pmSyn1-EBFP-Cre (addgene plasmid # 51507;
101 kindly donated by Hongkui Zeng [31]),were obtained from Addgene.
102
103 *Intracerebral injection*
104 Intracerebral injections of rAAVs were performed as previously reported [21]. Briefly, 1µl of viral
105 suspension with a titer of $3x10^{12}$ vg/ml and 1 µl of 1% of Fast Green were freshly mixed and 300
106 nl of the mixture was loaded into a pulled-glass capillary. Pulling parameters were optimized to
107 obtain a long and tapering capillary tip. Mice were pre-treated with buprenorphine (0.1 mg/kg)
108 and meloxicam (1 mg/kg) 20 min before being anesthetized with 5% sevoflurane /95% O_2 ; mice
109 were then positioned into a stereotactic frame (David Kopf) and kept under continuous

110 anesthesia with 3% sevoflurane/97% O_2. Mice were positioned on a heated pad connected to a
111 closed-loop system to maintain body temperature, monitored by a rectal probe, at 37°C. Upon
112 incision of the scalp, a burr hole was prepared using a hand-held microdrive aiming the LHA at
113 AP = -1.20, ML = -1.25, DV = -4.70 (according to Paxinos atlas, 2nd edition [32]) refined for the
114 mouse strain under consideration of the age).
115 Under visual control, the pulled-glass capillary (tip closed) was moved into the drilled hole and
116 gently pushed down to verify that meninges could be penetrated without deflection of the
117 capillary. Thereafter, the pulled-glass capillary was withdrawn and opened at the very tip by
118 gently touching with a microscissor. Before lowering the pulled-glass capillary to the final
119 position inside the brain, a thin layer of $DPBS^{+Ca/+Mg}$ was applied, generating a virus-free tip by
120 capillary force. Since brain tissue might absorb some of the liquid out of the pulled-glass
121 capillary by its own tissue/capillary force, during further movement, the pulled-glass capillary
122 was lowered not slower than 2 mm/s. The viral suspension was injected using a Picosprizer
123 microfluidic device; injection was performed during 5 min. The duration of one pulse was 10 ms;
124 since the opening diameter of each capillary could be slightly different, the injection pressure
125 was adapted (between 20 and 60 psi) to ensure a constant overall flow rate of 50-60 nl/min.
126 After injection, the capillary was kept in place for 15 min and then removed with a continuous
127 movement (1 mm/s). Remaining pressure in the capillary was released before withdrawing it to
128 prevent any residual virus suspension to be discharged into the capillary thread.
129
130 *Immunohistochemistry*

131 Mice (mSOD) were sacrificed at P (post-natal day) 40 (injection at P25) or at P110 (injection at
132 P95); Fus mice were injected at P255 and sacrificed at P270.
133 Mice were trans-cardially perfused with PBS and then 4% PFA in PBS; after 18h of post-fixation
134 in 4% PFA, brains were cryoprotected in 30% Sucrose/PBS, embedded in OCT and serially
135 sectioned using a *Leica CM1950 cryostat* into 70 µm sections from AP +2.6 mm to -3.0 mm as
136 previously reported [21].
137 The ZsGreen reporter did not require immunodetection since the native signal was very strong.
138 For dedicated experiments, immunostaining for SOD1 (Anti SOD1, Sigma-Aldrich, HPA001401,
139 1:500), misfolded SOD1 (Misfolded SOD1 (B8H10), MédiMabs, MM-0070-p, 1:250) and Fus (Anti
140 Fus, Sigma-Aldrich, HPA008784, 1:300) was performed.
141 Briefly, sections were blocked in blocking solution (3% BSA, 0.3% Triton in PBS) for 2h at room
142 temperature (rt). Primary antibody was diluted in blocking solution and incubated at 4°C for
143 72h. Secondary antibody (Invitrogen, Donkey anti-rabbit Alexa Fluor 568, # A10042; Donkey
144 anti-mouse Alexa Fluor 647, # A31571; anti-guinea pig 405) was applied diluted 1:500 in
145 blocking solution after three washing steps (PBS 20 min at rt) and incubated for 2h at rt.
146 Subsequently sections were washed three times again and mounted using Gold Antifade
147 Mountant (Invitrogen #P36930).
148
149 *Image acquisition*
150 Glass slides of serially-sectioned brains were first subject to visual assessment using a Leica
151 DMIL equipped with a 2.5x/0.07 objective; brains that were injected in the wrong location or
152 displayed obvious macroscopic artifacts were excluded at this stage and not processed further.

153 The remaining set of brain sections were imaged in full using a slide-scanning microscope (Leica
154 DMI6000B) equipped with a 5x/0.12 objective and exposure time ranging between 300 ms (405
155 nm) to 800ms (647 nm). All images were saved at 15304 x 28295 resolution with 16-bit depth.
156 Images of the cortical areas immunostained for misfolded SOD1 were acquired using a Zeiss
157 LSM710 confocal laser scanning microscope equipped with a 20x air objective. In total, 15
158 optical sections each 1µm-thick were acquired for each region of interest.
159
160 *Neuron mapping*
161 A multiple software approach was devised to analyze brain section images and properly
162 parcellate and quantify projections from cortex to LHA; the pipeline is summarized in Fig. 1A
163 and is reported here in detail.
164 Anatomical annotation **–** Firstly, a custom *Fiji* [33] macro allowed extracting single brain sections
165 from whole microscopic slide images while appending serial numbers. Hands-on registration of
166 coronal brain sections was performed by means of *WholeBrain* package in *R* [34], laying its
167 foundations on the Allen Brain mouse reference Atlas (ABA version 2011 [35]). In view of
168 accounting for tilted sections (as compared to the original ABA coronal planes) and for biological
169 inter-individual brain differences, a series of easily recognizable anatomical landmarks were
170 chosen to appropriately map the regions of interest (ROIs) along the anterior-posterior (AP)
171 axis, as shown in the Supplementary Table 1. The stereotactic coordinates were determined
172 with *openbrainmap.org*.
173 Neuron segmentation **–** Despite the flexibility of the parameters of the built-in segmentation
174 functions in *WholeBrain*, a systematic underestimation of neuronal counts was noticeable in

175 areas with high neuronal density, such as the frontal cortex, whereas a systematic
176 overestimation of neuronal counts took place in areas with low neuronal density, due to the
177 inclusion of segments of dendrites as purported neurons. In order to avoid the warping of the
178 neuronal counts because of these opposing biases, a separate strategy was pursued for neuron
179 segmentation in single brain ROIs alone. RGB images with single region outlines were generated
180 as explained in https://gitter.im/tractatus/Lobby and imported in *Fiji* [33]. Another *Fiji* macro
181 was then designed to mask and resize the RGB image in order to have a perfect match of the
182 original high-resolution image, to convert the former to HSB Stack, recover the outline of the
183 brain ROI and use it to crop the latter.
184 *Ilastik* toolkit [36] subsequently served a double purpose. The Pixel Classification workflow
185 enabled to discriminate neurons (foreground) from neuron-devoid brain architecture
186 (background); the resulting binary images (Fig. 1A, 4.3) were fed to a final *Fiji* macro to crop
187 highly-resolved brain ROIs (Fig.1A, 4.2) to smaller ROIs containing neurons only (Fig.1A, 4.6) and
188 exclude brain ROIs without LHA-projecting *somata* from further analysis. This step proved
189 crucial to resort to a highly trained Cell Density Counting *Ilastik* suite, since brain architecture
190 removal reduced the chance of generating false positives and drastically lessened the burden on
191 the RAM.
192
193 *Ilastik training*
194 For both pixel classification and cell density counting workflows, σ values of 1.0, 1.6, 3.5 and 5.0
195 were selected for the following features: Gaussian Smoothing, Laplacian of Gaussian, Gaussian
196 Gradient Magnitude, Difference of Gaussian, Structure Tensor Eigenvalues, Hessian of Gaussian

197 Eigenvalues. Twenty randomly selected whole-section images were sufficient for Pixel
198 Classification training; batch processing generated simple-segmentation.tiff (Figure1, A, 4.3)
199 images.
200 On the other hand, the Cell Density Counting classifier required a total of 250 randomly selected
201 images for training. As displayed in figure 1B, after annotating 100 images the training effect
202 had already reached saturation. Since accuracy of less than 90% seemed not satisfying enough,
203 additional 150 images were annotated to tweak out a few more percentages in accuracy.
204 Furthermore, we adapted the parameters of the implemented *Random Regression Forest*
205 algorithm (described in more detail in [37]), namely number and maximum depth of the trees
206 (Ntrees = 20, MaxDepth = 80), achieving a final accuracy of 94% by comparing counts to a
207 selection of 100 randomly selected and manually counted images. Random sampling of
208 probability maps exported upon batch image processing provided a further quality control
209 (Fig.1A, 5.2).
210
211 *Determination of single brain region and injection site volumes*
212 Volume measurements were performed with yet another custom macro in *Fiji*, measuring the
213 area of individual scaled cropped.tiff images (Figure1, A, 4.2) and multiplying by the thickness of
214 a single section (70 µm). Injection site volumes were determined by manually defining their
215 cross-section in every brain slice at a set image contrast and once again multiplying such areas
216 for the section thickness. Brains with injection sites bigger than 1 mm^3, mislocalized position or
217 displaying a virus backflow (visible in dorsal regions with respect to the LHA) bigger than 10% of
218 the whole injection site itself were excluded from further analysis.

219

220 *Determination of misfSOD1 burden*

221 A dedicated macro in Fiji was used to create a selection of misfSOD positive cells by applying the
222 RenyiEntropy [38] thresholding and subsequent background subtraction (rolling ball radius = 20
223 px) and gaussian blurring (σ = 1). Afterwards, the area was measured by restoring the selection
224 in the original image

225

226 *MRI scanning of DTI data in ALS patients*

227 DTI scanning study included 83 ALS patients (58 ± 14 years, 49m, ALS-FRS-R 40 ± 6, disease
228 duration 19 ± 16 months) and 64 controls (52 ± 11 years, 33m) according to a standardized
229 protocol (for details see [39]). DTI data were acquired on a 3.0 T head scanner (Allegra, Siemens
230 Medical, Erlangen, Germany). The standardized DTI scanning protocol was as follows: 49
231 gradient directions (b = 1000 s/mm^2) including one b = 0 gradient directions, 52 slices, 96 x 128
232 voxels in-plane, slice thickness 2.2 mm, in-plane voxel size 2.2 mm x 2.2 mm, echo time 85 ms,
233 repetition time 7600 ms. All participating patients and controls provided written informed
234 consent for the study according to institutional guidelines. The study was approved by the
235 Ethical Committee of the University of Ulm (reference #19/12).

236

237 *DTI analysis*

238 The DTI analysis software Tensor Imaging and Fiber Tracking (TIFT [40]) was used for post
239 processing and statistical analysis as previously described [39]. In brief, stereotaxic
240 normalization to the Montreal Neurological Institute (MNI) space was performed iteratively

using study-specific templates. To map white matter microstructure, fractional anisotropy (FA) maps were calculated from the stereotaxically normalized DTI data sets of all subjects. A Gaussian filter of 8 mm full width at half maximum was applied for smoothing of FA maps for a good balance between sensitivity and specificity [41] and FA maps were corrected for the covariate age. Tractwise fractional anisotropy statistics (TFAS) was performed by statistically comparing the FA values between the two subject groups in a given tract system [42]. The following tract systems were focussed on: a tract from orbitofrontal regions to the hypothalamus (orbitofrontal-hypothalamic tract), a tract from the hypothalamus to the insula (insular-hypothalamic tract), the cingulate-hypothalamic tract, and the corticospinal tract as a reference. Consequently, a tract-of-interest (TOI) analysis allowed for quantification of microstructural alterations in these tract systems.

Statistical analysis

The statistical analysis was performed with the *GraphPad8* software suite. Comparison of the neuronal counts (absolute counts or normalized) was performed by two-way ANOVA (genotype x structure design) using Sidak´s post-hoc multiple comparisons correction; corrected p values are provided. Normalization was obtained dividing the absolute number of neurons in each structure for the total number of neurons counted in that brain and multiplying the ratio for 50,000. Comparison of total neuronal counts was performed by two-tailed unpaired Student´s t-test. Comparison of misfSOD1 burden was performed by one-way ANOVA with Tuckey´s post-hoc test.

263 **Results**

264 ***Enhanced semi-automated mouse brain segmentation with neuronal annotation for global***
265 ***quantification of projections with single-cell resolution.***

266

267 In order to build a quantitative and anatomically accurate map of projections from cortical and
268 subcortical areas to the lateral hypothalamus, first we set out to establish a reliable approach to
269 identify neurons and register their position within the structure classification of the Allen Brain
270 Anatomical reference Atlas (Fig. 1A). The image batch for software training was obtained by
271 injecting the retrograde rAAV2 (rAAV2-retro) into the LHA of two ZsGreen reporter mice. The
272 latter were sacrificed 15 days later and the fixed brain was serially sectioned in 70 µm-thick
273 sections; the whole glass slide with mounted sections was scanned using a Leica epifluorescence
274 microscope. Each atlas plate was warped onto the brain section by defining an appropriate
275 number of corresponding anatomical landmarks with *WholeBrain* (see the Methods section),
276 thereby matching the atlas coordinates with the actual brain sections and allowing a proper
277 anatomical annotation (Fig. 1A, 2). Single structure outlines (cortical layers, subcortical
278 structures, e.g. fig. 1A, 4.1) were extracted using a dedicated *R* script, size-corrected and re-
279 overlapped onto the original image in *Fiji*; the corresponding area of the original image was then
280 cropped (Fig. 1A, 4.2), resulting in the unpacking of the original single-section into several
281 hundreds cropped pictures (each image was coded to be later identified), resulting in >100,000
282 pictures per brain. In order to identify and count the number of neurons in each fragment,
283 *Ilastik* software suite was employed. Simple foreground/background segmentations were
284 generated by resorting to the pixel classification workflow. This allowed to automatically clear

285 most of the brain autofluorescence background in *Fiji* (Fig. 1A, 4.6). This step enabled the
286 improvement of the discrimination of few ZsGreen+ neurons in ROI containing many more
287 dendrite stretches and artifacts, and also reduced the computational burden placed on *Ilastik*
288 cell density classifier and therefore minimizing the chance of generating artifactual counts.
289 *Ilastik cell density* classifier was trained with 250 randomly selected ROI images that were
290 annotated by a human operator; the accuracy of software reached 86% after 100 images and
291 achieved a final 94% peak (Fig. 1B) by improving the performance of the *Random Regression*
292 *Forest* algorithm with 150 additional images and tuning its parameters (trees number and
293 depth; see Methods). The whole procedure was then sequentially implemented so that
294 neuronal counts for each picture from every section were annotated and logged together with
295 the anatomical location within the hemisphere and the brain section as well as with the rostro-
296 caudal serial number of the section itself.
297
298
299
300
301
302

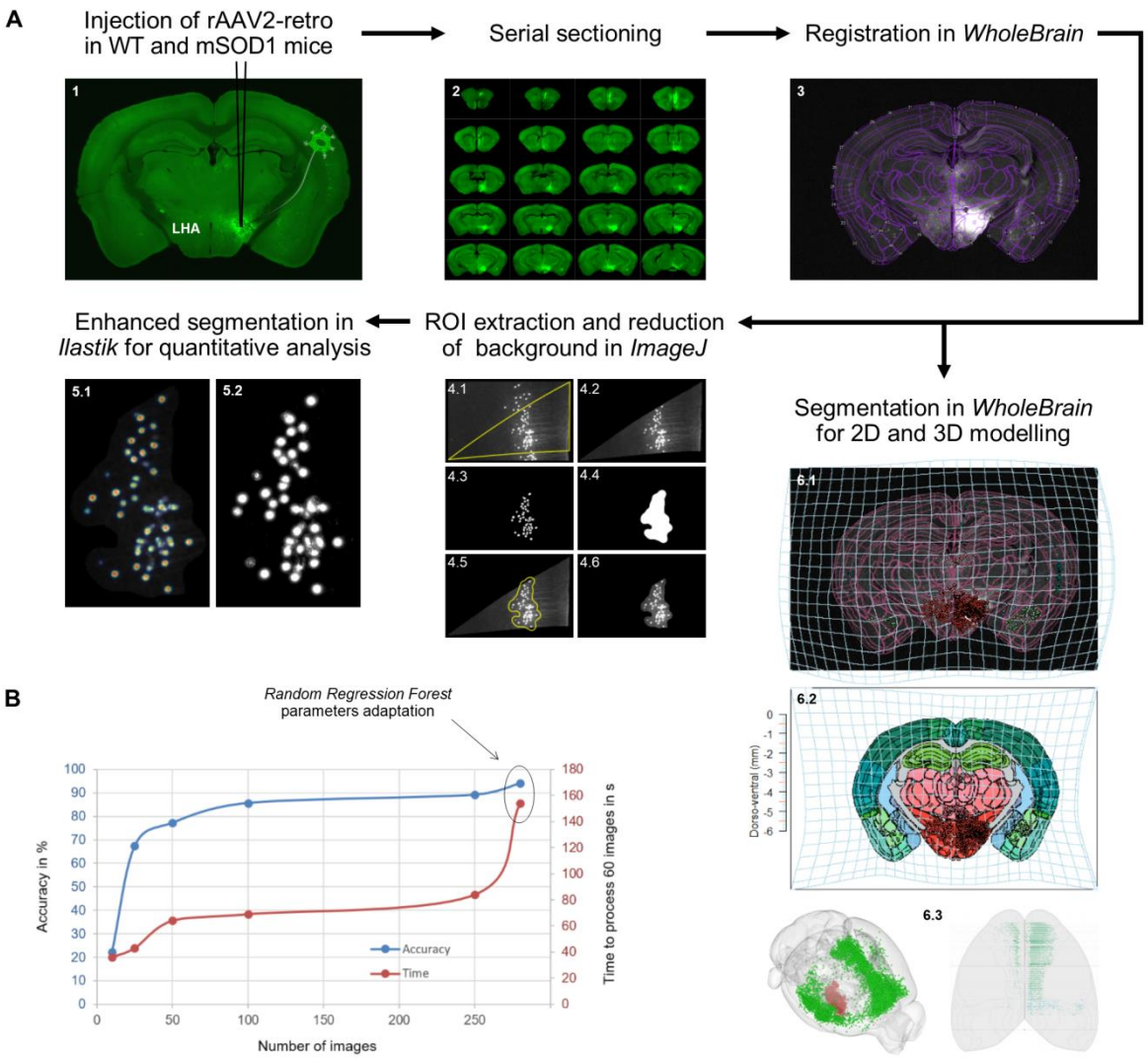

Figure 1: Pipeline for the quantitation of forebrain projections to LHA. A: Neurons projecting to LHA are identified by injecting rAAV-retro encoding Cre in the LHA of WT (or mSOD1) carrying a floxed ZsGreen reporter allele (panel 1). Brains are serially sectioned (2) and each section is manually registered in *WholeBrain* (3). To obtain a precise quantification of the neurons in each anatomical structure, registered sections are parcellated and background-corrected in *ImageJ* (panel 4) and the parcellated images are segmented using a purpose-trained *Ilastik* (density counting workflow) (5) to obtain the final neuronal counts per image. The *WholeBrain* dataset is also used to derive an independent anatomical annotation in the Allen Brain Atlas (backward warp transform field (atlas plate to section) 6.1, forward warp transformation field (section to atlas plate) 6.2) and 3D reconstructions (6.3). B: Training of *Ilastik* cell density counting. Accuracy improvement of the classifier according to the amount of images used for training. The increasing need of computing power is indicated by the time needed to process 60 Images. Accuracy was calculated by comparing randomly selected and manually counted images. Using a total of 250 images and adapting the parameters for the *Random Regression Forest*, a final accuracy of 94% was achieved.

319 ***Disrupted cortico-hypothalamic projections in symptomatic mSOD1 ALS mice***

320 We exploited our enhanced registration-segmentation-annotation pipeline to establish whether
321 the large-scale architecture of the projections to LHA was altered in the mSOD1 mice at a
322 symptomatic stage (i.e., when body weight loss has appeared and clinical score is 2). To this aim,
323 20 mSOD1/ZsGreen+ and 20 WT/ZsGreen+ mice were injected at the age of P95 with rAAV2-
324 retro [30] encoding for Cre under the human synapsin promoter in the Lateral hypothalamic
325 area (LHA; Fig. 2A). All neurons projecting to the site of injection would take up the rAAV2-retro,
326 express the Cre recombinase and appear ZsGreen+. Mice were sacrificed 15 days later. Upon
327 serial sectioning, a series of quality control criteria were applied and brains displaying i)
328 improper location of the injection site ii) injection volume larger than the boundaries of the LHA
329 iii) large number of neurons infected along the thread of the injection capillary iv) low (<25,000)
330 overall number of ZsGreen+ neurons were excluded from further analysis. Six brains for each
331 genotype were then considered for further quantification. These brains were randomly divided
332 in two cohorts: cohort 1 was subjected to *WholeBrain* parcellation and cohort 2 was left for
333 confirmation (see below). Once cohort 1 brains were processed through the *WholeBrain*-
334 registration and annotation pipeline, we identified an average of about 50,000 neurons
335 projecting to the LHA in WT mice; when the brainstem was excluded (because anatomical
336 annotation of brainstem nuclei was judged unreliable based on visual inspection of the
337 *WholeBrain*-overlapped images), we identified 84 cerebral areas projecting to the LHA (full list
338 with absolute and normalized neuronal counts is provided in the Supplementary Table 2).
339 Projections were identified from a large fraction of the forebrain, with the largest component
340 provided by limbic areas such as Anterior Cingulate Area (ACA), Prelimbic Cortex (PL),

341 InfraLimbic Area (ILA), Agranular Insula (AI), as well as from subcortical structures belonging to
342 the limbic system such as Basolateral and Basomedial Amygdala (BLA and BMA, respectively).
343 Intriguingly, substantial projections were identified from motor areas (primary and secondary),
344 from primary sensory areas (gustatory, auditory, olfactory/piriform, visual cortex) and from
345 basal ganglia (Dorsal Putamen, DP), underscoring the breath of integration taking place in LHA.
346 The same structures appeared to project to LHA from ipsilateral and contralateral hemispheres,
347 although the contralateral contribution appeared to be substantially smaller (approx. 40,000
348 neurons from the ipsilateral hemisphere vs 10,000 from the contralateral in WT animals).
349 In order to obtain a pertinent comparison (i.e., excluding areas with counts <100 neurons) of
350 projections in WT and mSOD1 mice, we contrasted the absolute neuronal counts in 28 areas
351 (accounting for approx. 50% of the total projections, maintaining ipsi and contralateral dataset
352 distinct; PL and orbitomedial cortex as well as lateral/ventrolateral orbitofrontal cortex -ORBl/vl-
353 and AI were grouped together due to the uncertainty in establishing their borders and in
354 agreement with functional similarity. While the overall pattern of projections to LHA in
355 symptomatic mSOD1 mice was comparable to the WT ones, the cumulative absolute counts of
356 ZsGreen+ neurons for the 28 structures were significantly increasedin the mSOD cohort
357 considering the absolute counts ($p=0.02$; Supplementary Fig. 1-A). We contrasted the absolute
358 counts for each of the 28 areas in WT and mSOD1 mice (Supplementary Fig. 1- 1B). Two-way
359 ANOVA revealed a significant effect of genotype ($F_{1,112}=105.70$, $p<0.0001$) and post-hoc analysis
360 (Sidak´s multiple comparisons test) revealed significant expansion of the projections from ACA
361 ($p<0.0001$), ILA ($p=0.009$), ORBl/vl+AI ($p<0.0001$), Tenia Tecta (TT; $p=0.0365$), secondary motor
362 cortex (MOs, $p<0.0001$) and piriform cortex (PIR; $p=0.0005$). In order to compensate for the

363 variable total number of infected neurons in each individual brain, we then normalized the
364 absolute counts of neurons projecting to LHA to a nominal of 50,000 neurons, so to compute
365 the relative contribution of each area to the total input to LHA. Upon normalization, the 28
366 areas in object amounted for a comparable total number of neurons (Fig. 2B). Two-way ANOVA
367 on normalized data revealed once again a significant effect of genotype ($F_{1,112}$= 7.31, p=0.0079)
368 and post-hoc analysis revealed a significant increase in projections from ORBl/vl+AI (p=0.0012)
369 and from MOs (p=0.0006; Fig. 2C; also visualized in the 2D projections, Supplementary Fig. 1-C-
370 D as well as in the 3D Wholebrain reconstruction, Fig. 2D). The remaining 26 structures
371 displayed only non-significant trends toward expanded projections (PIR: p=0.21; ILA: p=0.32) or
372 no difference in the size of the neuronal population projection to LHA (Fig. 2C). When the
373 projections from the contralateral hemisphere were contrasted, we detected an effect of
374 genotype in the absolute counts (two-way ANOVA $F_{1,112}$= 31.49 ; p<0.0001) that was traced in
375 post-hoc test (Sydak´s) to a significant expansion of projections from ACA (p=0.0008), ILA and
376 PL+ORBm (both p<0.0001) (Supplementary Fig. 2- 2A-B). However, when the absolute counts
377 were normalized to account for the total number of ZsGreen$^+$ neurons in each brain, no
378 significant differences were identified between the genotypes (two-way ANOVA, $F_{1,112}$= 0.31,
379 p=0.57; Supplementary Fig. 2-C).
380
381 Since mice with neurodegenerative phenotypes may display cortical atrophy [43], we used the
382 *WholeBrain* registration to measure the volume of each cortical structure and compensate for
383 eventual volume loss. Indeed, we identified a significant loss of volume in mSOD1 mice (two-
384 way ANOVA $F_{1,112}$=28.80, p<0.0001) which was traced by post-hoc test (Sidak´s.) to the atrophy

of MOp (p=0.008) and SS (p<0.0001) with only a trend seen for MOs (p=0.33) (Supplementary Fig. 3). Notably, ORBl/vl+AI and MOs did not display significant changes in volume.

Thus, in symptomatic mSOD1 mice (displaying the hypermetabolic phenotype), a substantial remodeling of cortico-hypothalamic projections takes place, in particular from ORBl/vl+AI and MOs.

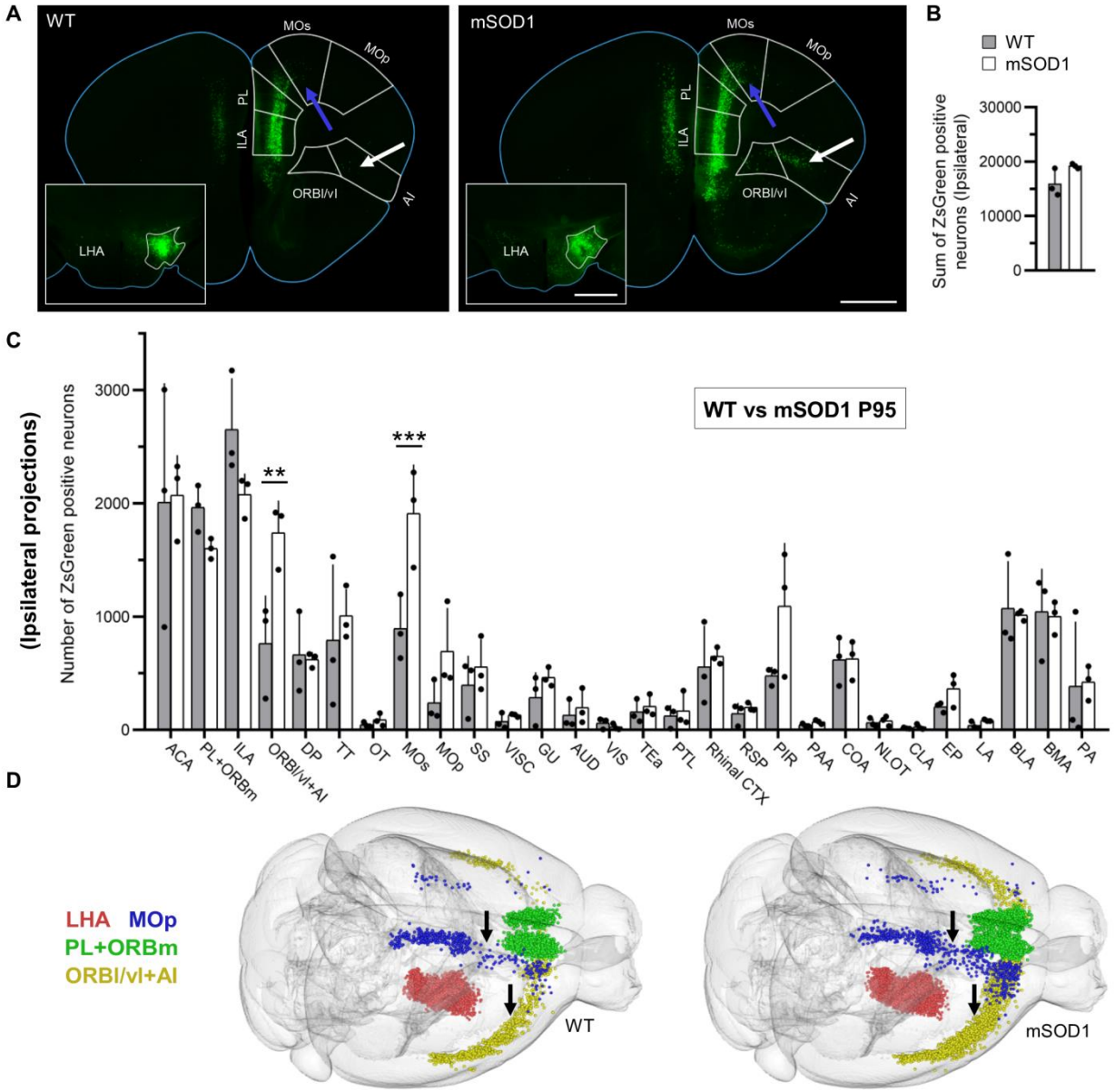

392 ***Figure 2***: Altered cortico-hypothalamic projection pattern in mSOD1 mice at P95. A:
393 Representative frontal brain sections of WT and mSOD1 mice depicting projections from
394 ORBl/vl+AI (significantly increased, arrow), PL+ORBm, ILA, ACA, MOs and MOp to LHA. Inset:
395 representative injection sites in LHA for WT and mSOD1 mice. White outlines represent LHA
396 boundaries. B: Sum of neurons projecting from selected 28 areas. No difference is detected in
397 the summarized number of neurons projecting to LHA in WT and mSOD1 from the ipsilateral
398 hemisphere (n=3). C: Quantification of the number of neurons (normalized for total neuronal
399 counts) projecting to LHA from 28 brain structures in WT and mSOD1. A significant increase in
400 projections from ORBl/vl+AI (p=0.0012) and from MOs (p=0.0006) is detected. D:
401 Representative *WholeBrain* volume reconstructions of neurons projecting to LHA in WT and
402 mSOD1 mice. Expansion of projections from MOs (blue) and ORBl/vl+AI (yellow) are visible
403 (arrows). Bars show mean ± SD. Scalebars 1 mm . *$p < 0.05$, ***$p < 0.001$, ****$p < 0.0001$.
404

405 ***Validation of cortico-hypothalamic projections abnormalities in independent operator-***
406 ***registered brain cohorts***

407 Since the identification of different cortical and subcortical areas was based on the assumption
408 of the overall similarity of the brain of mSOD1 and WT mice, we took into consideration the
409 possibility that biases in the identification of anatomical areas could have been introduced by
410 *WholeBrain* (e.g., because of atrophy), thereby mis-attributing neurons to cortical areas.
411 Therefore, we set out to validate our findings using the brain cohort 2 (n=3 for WT and mSOD1;
412 LHA injection; Supplementary Fig. 4-A). These brain images were subjected to manual
413 registration, i.e. each anatomical structure and cortical area was identified by a genotype-blind
414 operator using structural landmarks (Supplementary Table 1) and individually cropped out of
415 each image of each section of the brain. This approach was substantially slower than the
416 registration by *WholeBrain* (it required >500h of operator´s work time for the whole dataset to
417 be registered and cropped). The individual pictures cropped out of the brain images were then
418 subject to neuronal counts by *Ilastik* (since the accuracy and reproducibility of this step was
419 already established and quantified). In the manually-annotated dataset, the total number of

420 neurons projecting to LHA was found to be not significantly different in the mSOD1 compared to
421 the WT (Supplementary Fig. 4-B). First, we considered the absolute neuronal countings: the
422 contrast of the two genotypes (ipsilateral hemisphere) revealed a statistically significant
423 difference (two-way ANOVA $F_{1,112}$=6.28 ; p=0.0136) which was further explored in post-hoc
424 comparison (Sydak´s) revealing a significant expansion of projections from ORBl/vl+AI in mSOD1
425 mice (p=0.035) (Supplementary Fig. 4-C). Upon normalization we once again detected a
426 significant effect of genotype (two-way ANOVA $F_{1,112}$=23.78 ; p<0.0001) with post-hoc revealing
427 significant differences in ORBl/vl+AI (p<0.0001), ILA (p=0.001) and PIR (p<0.0001)
428 (Supplementary Fig. 4-D). When the projections from the contralateral hemisphere were
429 considered, no overall, genotype specific or area correlated effect was found in the absolute
430 counts (Supplementary Fig. 5-B); however, upon normalization, a statistically significant loss of
431 projections from PL+ORBm was identified (p<0.0001), together with a strong trend toward
432 increased projections from ORBl/vl+AI (p=0.072) (Supplementary Fig. 5-C). Thus, the manually-
433 registered dataset displayed substantial similarities with the *WholeBrain*-registered dataset
434 (expansion of the projections from ORBl/vl+AI) but also a major discrepancy: increased
435 projection from ILA to LHA in the manual dataset and no difference in MOs projections, whereas
436 the opposite was detected by *WholeBrain*. Upon closer inspection of MOs projection to LHA we
437 realized that the boundaries of MOs and ILA display a high degree of subjectivity when manually
438 drawn and it is highly likely that MOs neurons were allocated to adjacent areas in the same way
439 ILA was moved to neighboring areas in the dataset parcellated by the human operator.
440 Nevertheless, the manually-registered independent dataset confirmed the expansion of
441 projections from AI/ORBvl to LHA.

442

443 ***Unaltered projections to LHA in early presymptomatic mSOD mice***

444 Remodelling of large-scale cortical circuits has been previously reported [21] and appears to
445 progress over time; nevertheless, early signs of increased projections from somatosensory
446 cortex (SS) to primary motor cortex (MOp) were detected already at early presymptomatic
447 stages. We set out to verify if the increased projections from AI/ORBvl appeared only late, in
448 coincidence with the appearance of the metabolic phenotype, or if they were present already at
449 presymptomatic stage (and possibly of developmental origin). To this aim, we injected rAAV2-
450 retro in the LHA of WT or mSOD1 at the age of P25 (Supplementary Fig. 6-A) and sacrificed the
451 mice at P40. After quality control, we assessed the forebrain projections to LHA in the two
452 genotypes (n=3 for each). The overall pattern of projections to LHA at P25 was comparable to
453 the one observed at P95 and there was no difference in the absolute number of neurons
454 projecting to LHA in the two genotypes (Supplementary Fig. 6-B). The direct contrast of the two
455 genotypes for the absolute and relative contribution of 28 selected ipsilateral structures
456 revealed a genotype effect in absolute (two-way ANOVA: $F_{1,112}$= 12.55 ; p=0.006) but not in the
457 normalized dataset (two-way ANOVA: $F_{1,112}$= 1.83 ; p=0.1779). However, in both cases the post-
458 hoc comparison did not reveal any significant difference between the two genotypes in any of
459 the considered structures (Supplementary Fig. 6-C,D). Likewise, no statistical difference was
460 found in the sum of projection from the contralateral hemisphere in absolute counts
461 (Supplementary Fig. 7-A), but significant increase in projections from ACA was identified
462 (p=0.0078) (Supplementary Fig. 7-B). Nevertheless, this difference disappeared after
463 normalization (Supplementary Fig. 7-C) and no differences are perceptible in the 3D brain

464 reconstructions (Supplementary Fig. 7-D). These findings suggest that altered AI/ORBvl
465 connectivity to LHA arises during disease progression and it is not a developmental feature of
466 mSOD1 brain architecture.
467
468 ***ALS-related pathology in the AI/ORBvl of mSOD1 mice***
469 We further investigated the degree of involvement of cortico-hypothalamic projections in ALS
470 by assessing the burden of misfolded SOD1 pathology in cortical areas projecting to LHA, in
471 particular those displaying altered connectivity compared to WT animals. We injected WT or
472 mSOD1 mice with rAAV2-retro in LHA at P95 and sacrificed them at P110. Brain sections
473 encompassing MOp, AI/ORBvl, PL+ORBm, (SS) were immunostained with an antibody
474 recognizing the misfolded conformation of SOD1 (B8H10 [44]) (Fig. 3A-B). The total burden of
475 misfSOD1 was different across the cortical areas (one-way ANOVA $F_{3,20}$=51.26, p<0.0001; MOp
476 vs. ORBl/vl+AI p<0.0001, MOp vs. PL+ORBm p<0.0001, SS vs. ORBl/vl+AI p=0.0014, ORBl/AI vs.
477 PL+ORBm p=0.0006), with MOp displaying the highest burden compared to SS but with
478 ORBl/vl+AI displaying a significantly higher burden than areas showing no increase in
479 projections such as SS or PL+ORBm (Fig. 3A-B). Interestingly, neurons projecting from MOs to
480 LHA display high levels of misfSOD1 accumulation, whereas this is not true for neurons
481 projecting from PL+ORBm and ORBl/vl+AI (Fig.3A).
482
483
484
485

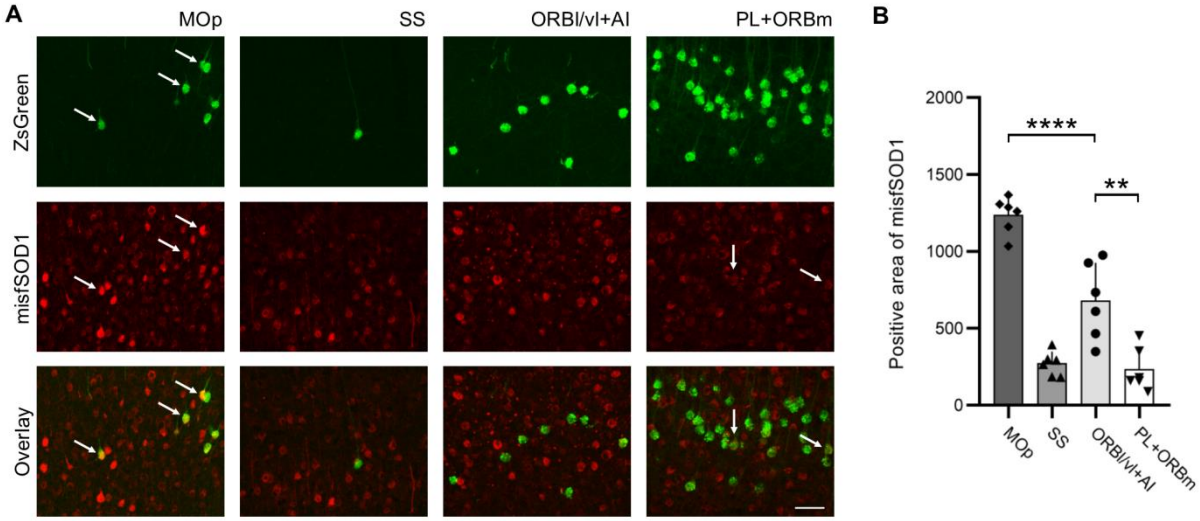

Figure 3: Significant misfolded SOD1 burden in ORBl/vl+AI in mSOD1 mice. A: Representative images of misfSOD1+ cells in MOp, SS, ORBl/vl+AI and PL+ORBm; ZsGreen^{+} neurons projecting to LHA show a strong misfSOD1 burden in MOp (arrows). Other structures show no double positive neurons (SS,ORBl/vl+AI) or weak mSOD burden (PL+ORBm; arrows). B: Burden of misfolded SOD1 (detected by the B8H10 antibody) in MOp, SS, ORBl/vl+AI and PL+ORBm. ORBl/vl+AI displays a burden significantly higher than SS or PL (p=0.0014 and p=0.0006 respectively; areas with unchanged connectivity to LHA) but significantly lower than MOp (p<0.0001). Bars show mean ± SD. Scalebars 50 µm. $^{**}p < 0.01$, $^{****}p < 0.0001$.

Distinct pattern of altered cortical projections to LHA in Fus mice

We further explored the alteration of projections to LHA in ALS in an independent ALS model, the kiFUS mouse. Of note, the kiFUS mouse differs from the mSOD1 mouse because it does not display an overt body-weight phenotype [45] and shows a more limited loss of spinal motoneurons and slower progression [29]. We proceeded with a similar experimental design as for the mSOD1 mice; however, since kiFUS mice display spinal motoneuron loss not before 9-10 months of age, we considered the P255 as “early symptomatic” stage. Therefore, kiFUS mice and their own WT littermates were injected at P255 into the LHA (Fig. 4A and sacrificed at P270 (n=4 for each group). Once again, there was no difference in the overall number of neurons projecting to LHA across the forebrain in absolute counts (Supplementary Fig. 8-A). When the

506 absolute neuronal counts of each of the 28 areas were contrasted, we detected a significant
507 effect of the genotype (two-way ANOVA $F_{1,166}$=8.583 ; p=0.0039) and post-hoc comparison
508 revealed a significant decrease in kiFUS in projections from ACA (p=0.0385), MOs (p<0.0001)
509 and strong trends for MOp (p=0.1543) and SS (p=0.0848) (Supplementary Fig. 8-B). Upon
510 normalization for 50,000 neurons, a significant difference in MOs was still detected (p<0.0001)
511 together with strong trends for ACA (p=0.1639) and MOp (p=0.136) (Fig. 4B-C and 2D models in
512 Supplementary Fig. 8-C,D). Interestingly, a significant genotype effect was also found in the
513 contralateral hemisphere both in absolute (Supplementary Fig. 9-A,B) and normalized data
514 (Supplementary Fig. 9-C) (two-way ANOVA, $F_{1,166}$= 6.57 ; p=0.0112 and $F_{1,166}$= 4.48 p=0.0356,
515 respectively) and differences were revealed by post-hoc analysis in loss of projections from ACA
516 (p=0.0121 and p=0.0137 in absolute counts and normalized, respectively) and ILA (p=0.0474) in
517 the absolute counts only. Of note, projections from AI/ORBvl were not affected (neither from
518 ipsilateral nor from contralateral). The significant loss of MOs neurons projecting to LHA was
519 especially affecting the most rostral part of MOs, as demonstrated by the 3D reconstruction
520 model of the mouse brain (Fig. 4D). Thus, distinct ALS models with divergent metabolic
521 phenotype display different patterns of altered projections to LHA.
522
523
524
525
526
527

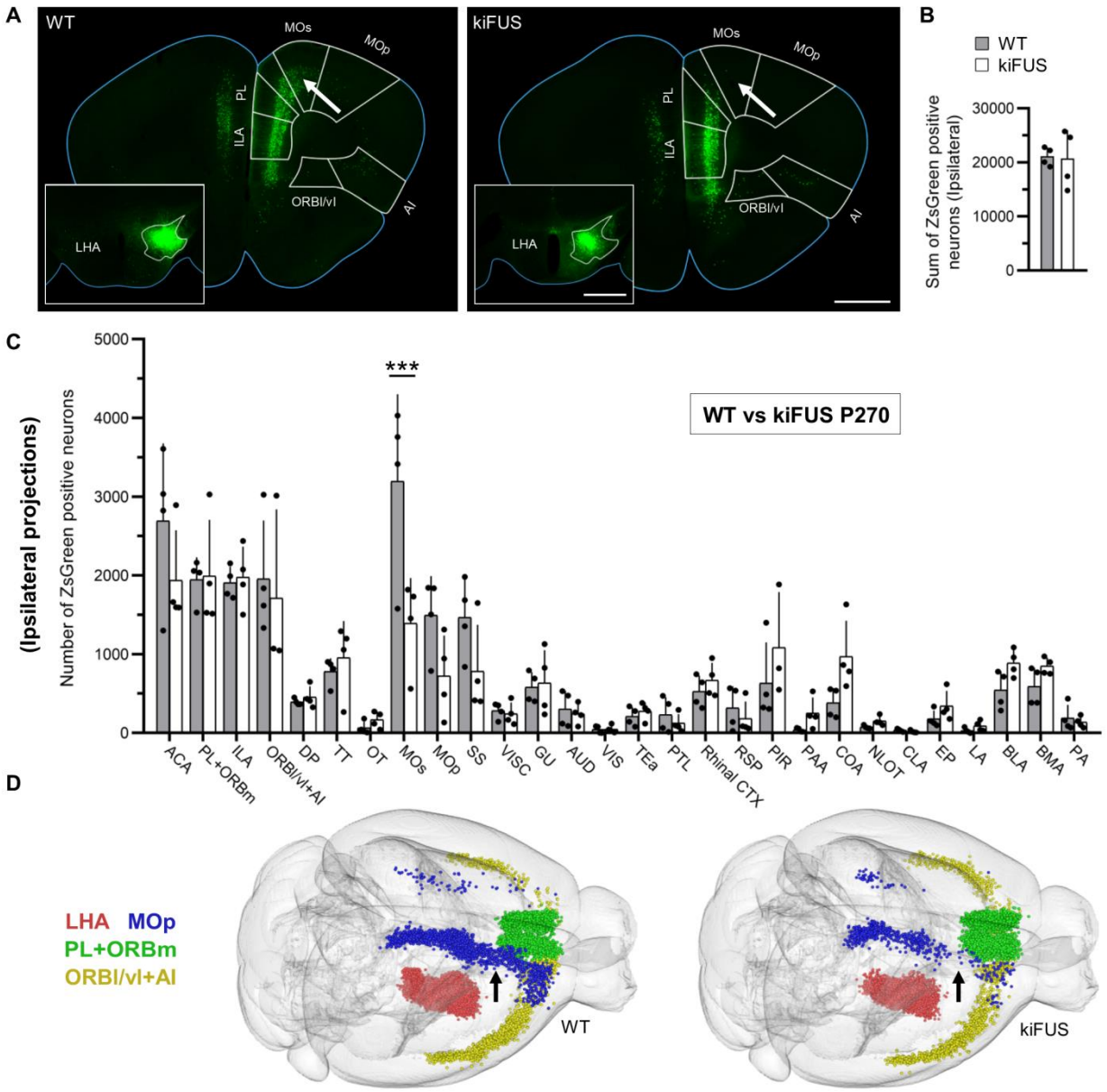

528

529 ***Figure 4***: Altered cortico-hypothalamic projection pattern in kiFUS mice at P270. A:
530 Representative frontal brain sections of WT and kiFUS mice depicting projections from MOs
531 (significantly decreased, arrow), PL+ORBm, ILA, ACA, and MOp to LHA. Inset: representative
532 injection sites in LHA for WT and kiFUS mice. White outlines represent LHA boundaries. B: Sum
533 of neurons projecting from selected 28 areas. No difference is detected in the summarized
534 number of neurons projecting to LHA in WT and kiFUS from the ipsilateral hemisphere (n=4). C:
535 Quantification of the number of neurons (normalized for total neuronal counts) projecting to
536 LHA from 28 brain structures in WT and kiFUS. A significant decrease in projections from MOs
537 ($p<0.0001$) and trend toward decrease projection from ACA ($p=0.1639$) and MOp ($p=0.136$) is
538 detected (n=4). D: Representative *WholeBrain* volume reconstructions of neurons projecting to

539 LHA in WT and kiFUS mice. Loss of projections from the anterior part of MOs (blue) is visible.
540 Bars show mean ± SD. Scalebars 1 mm. *$p < 0.05$, **$p < 0.01$, ****$p < 0.001$.
541

542 ***DTI-MRI reveals altered orbitofrontal-hypothalamic tract in ALS patients.***

543 Finally, we set out to investigate if the selective disturbance in cortico-hypothalamic projections
544 from AI, ORBvl and PL observed in the mSOD1 mice could also be observed in human ALS
545 patients. To this aim, we elected to use a 3T DTI-MRI dataset involving 83 ALS patients and 64
546 healthy subjects [39].Four white-matter tracts were taken into consideration: the orbitofrontal-
547 hypothalamic tract, the insular-hypothalamic tract, the cingulate-hypothalamic tract (Fig. 5) and
548 as reference the corticospinal tract which is known to be substantially altered in ALS patients
549 [39]; the three tracts converging on the hypothalamus were selected because they provided the
550 closest possible match (when accounting for the different anatomy) for the structures
551 investigated in the mouse model and because of their reproducible and unequivocal
552 identification in DTI datasets. We identified a significant decrease in Fractional Anisotropy (FA)
553 of the orbitofrontal-hypothalamic tract in ALS patients ($\Delta FA = -0.008 \pm 0.003$; $p<0.05$), with a
554 magnitude approximately one-third of the FA loss in the corticospinal tract ($\Delta FA = -0.025 \pm 0.003$;
555 average±SEM, $p<0.001$; Fig. 5). For the cingulate-hypothalamic and insular-hypothalamic tracts,
556 smaller FA losses were detected, which did not reach statistical significance. Thus, disturbances
557 of cortical projections to hypothalamus are not unique characteristics of the mSOD1 murine
558 model of ALS but constitute a previously unrecognized architectural phenotype shared by
559 human ALS patients.
560
561

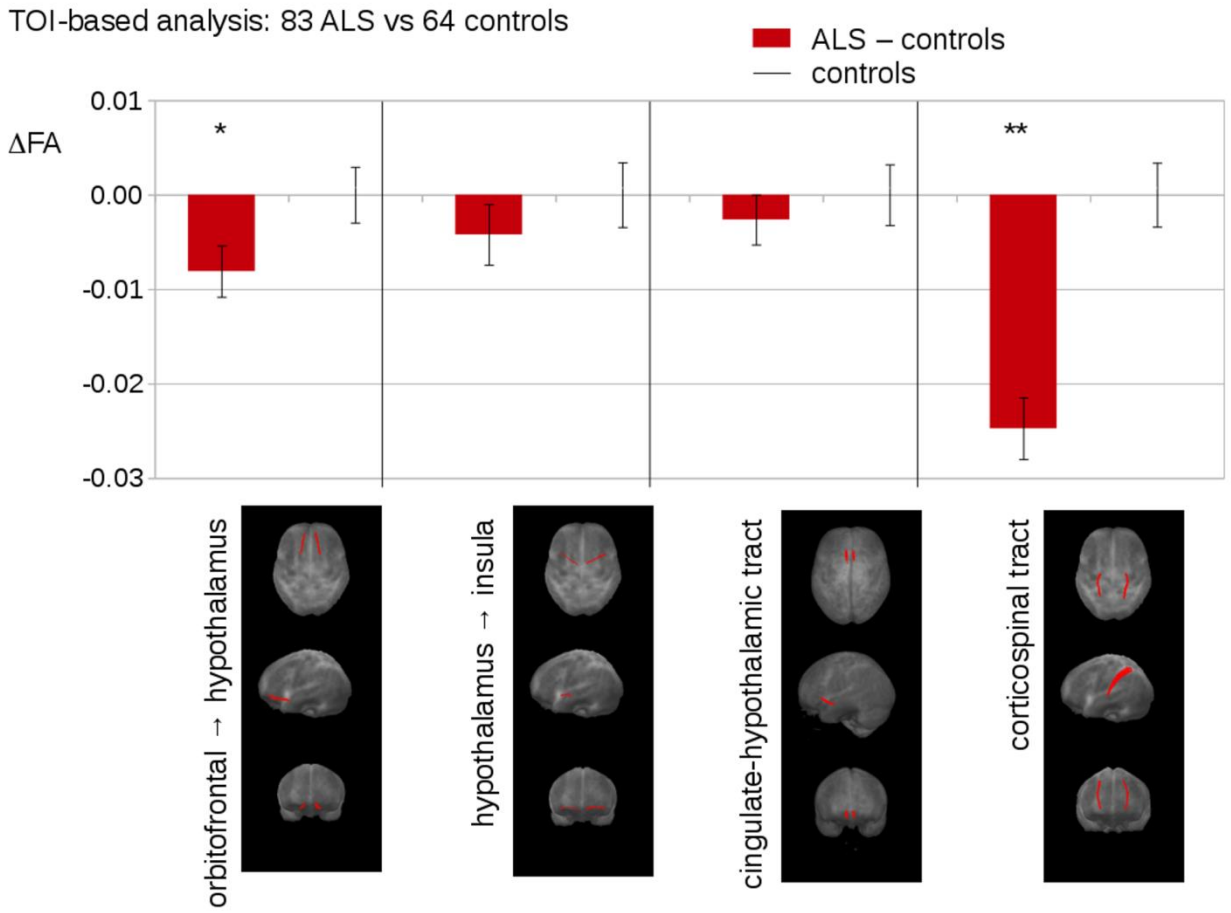

Figure 5: Tract of Interest (TOI)-based analysis of DTI data from 83 ALS patients vs 64 controls. Upper panel: differences of mean fractional anisotropy (FA) values between ALS patients and controls. Lower panel: projectional views (axial, coronal, sagittal) of tract systems used for TOI analysis. TOI – tract-of-interest; *p < 0.05; **p < 0.001; error bars are the standard error of the mean (SEM).

Discussion

Here we provide converging evidence from ALS mouse models and human imaging datasets of the involvement of large-scale projections to LHA in ALS, in particular the disruption of connections from Orbitofrontal Cortex and/or Agranular Insula to LHA. This effect is independent of systematic biases introduced by software or human operators in the registration, does not appear to be an intrinsic developmental defect and it is not detected in an independent ALS model devoid of metabolic phenotypes. The findings in the murine model

576 display striking similarity to the disruption of the orbitofrontal-hypothalamic tract identified in a
577 large dataset of DTI-MRI of ALS patients.
578
579 Hypermetabolism in ALS has been repeatedly reported in human patients [9-13] as well as in
580 some, but not all, ALS murine models [14] and, notably, it appears to develop over time and
581 may predate the clinical onset of disease by several years [3, 46]. Nevertheless, the mechanisms
582 for this clinical manifestation of ALS are unclear.
583 Direct involvement of the hypothalamus has been hypothesized on the basis of the role of this
584 structure as the main central controller of energy homeostasis, feeding and satiety [47], has
585 been supported by evidence of reduced hypothalamic volume in ALS patients [48] and by the
586 detection of ALS-related TDP-43 pathology in a subset of ALS patients hypothalami [49].
587 Neurochemical abnormalities, such as reduced MCH expression, have been reported in mutant
588 SOD1 murine models [50]. However, these signs of intrinsic hypothalamic disturbance are not
589 mutually exclusive with the hypothesis that large-scale hypothalami circuits may be
590 dysfunctional, too. Disruption within the larger circuit regulating hypothalamic function, which
591 include insular, motor, orbitofrontal and limbic areas, may contribute to the hypothalamic
592 dysregulation by altering the equilibrium of the different inputs. Indeed, changes in neuronal
593 activity in hypothalamus may produce substantial modifications of the neurochemical identity
594 of local subpopulation, including switch in type of neurotransmitter released [51]. Here we
595 demonstrate that besides any pathology intrinsic to the hypothalamus, the disease
596 pathophysiology involves a substantial quantitative change in the inputs that hypothalamus

597 receives, particularly from agranular insula and ventrolateral orbitofrontal cortex. This
598 remodeling process coincides with the onset of body weight loss in mSOD1.
599 Notably, the circuit involving projections from orbitofrontal cortex and agranular insula to
600 lateral hypothalamus is conserved from mice and rats [52, 53] to marmosets [54] and macaques
601 [55] to humans, thus validating mouse as a model organism. Nevertheless, the murine
602 orbitofrontal cortex (including ventral and ventrolateral) and agranular insula are considered
603 homologous of orbitomedial cortex in primates [56], so that the study the orbitofrontal-LHA
604 tract in our DTI tracing study is located more medially than the ORBl/vl+AI complex in the
605 mouse brain.
606
607 Remarkably, altered projections from AI/ORBvl in mSOD1 mice correspond to reduced FA in the
608 orbitofrontal-hypothalamic (but not insular-hypothalamic) tract in humans. Although it is
609 noteworthy that abnormalities appear in the same brain structures in animal models and
610 patients with ALS, the closer examination of the findings reveal that in the murine model an
611 actual expansion of projections is detected whereas decreased FA in DTI is usually interpreted
612 as loss of integrity of axons or myelinated tracts [57]. However, it must be stressed that
613 $SOD1^{(G93A)}$ displays a fast progression and becomes symptomatic at a comparatively young age,
614 when the potential for compensatory sprouting after degeneration may be larger than in older
615 human patients (hence, the expansion of the projections). Thus, in human patients the DTI may
616 reveal a change in microstructural integrity resulting from axonal loss but would be unable to
617 detect any increase in the size of axonal arborization.
618

619 To the best of our knowledge, there is no demonstration that the orbitofrontal cortex and/or AI
620 can directly regulate metabolic rates. It must be emphasized, though, that lesion studies of
621 these structures have not included a rigorous, long-term testing of body-weight dynamics and
622 inactivation studies have been performed only in short-term settings [58-60]. On the other
623 hand, OFC and AI are involved in processing food characteristics, such as taste, smell and
624 texture [61] and display a differential response to caloric content of food depending on the
625 satiety of the subject (at least in humans: [62, 63]). Thus, it is conceivable that altered
626 connectivity between vlORB/AI and LHA may provide the latter with incorrect inputs regarding
627 the nutritional content of food, contributing to the dysregulation of body metabolic rates. At
628 least in human subjects, reduced volume of grey matter and altered microstructural integrity
629 (measured by apparent diffusion coefficient) in orbitofrontal cortex have been observed in
630 obese patients [64-66], strengthening the link between dysfunction in orbitofrontal cortex and
631 body weight.
632
633 Unexpectedly, our retrograde projection mapping strategy has consistently identified
634 projections from primary and secondary motor cortex to LHA, which appear to be affected by
635 the disease process both in mSOD1 and in kiFUS. This connectivity appears to be reciprocal,
636 since LHA projections to motor cortices have also been reported [21]. These connections cannot
637 be easily discounted as artifacts due to the proximity of LHA to the corticospinal tract, since they
638 appear to originate from both ipsi and contralateral hemispheres. It is conceivable that LHA may
639 receive inputs relaying the average motor activity performed or planned and may adjust energy
640 balance accordingly; disruption of connectivity between motor cortex and hypothalamus may

641 leave the latter “free running”, without a proper estimate of current motor activity.
642 Alternatively, it is possible that any pathogenic event in motor cortex (propagating prionoids or
643 abnormal activity patterns) may propagate to hypothalamus and drive its dysfunction and
644 degeneration (as suggested for spinal cord [67]).
645
646 **Conclusion**
647 Our findings suggest that disruption of large-scale circuits providing input to LHA may contribute
648 to generate the metabolic phenotype observed in ALS; in particular, we have identified the
649 orbitofrontal-hypothalamic tract as a site of convergence of mouse projection data and human
650 tracing data, which may open up an independent approach to evaluate non-motor prognostic
651 features in ALS.
652
653 **Declarations**
654 *Acknowledgements*
655 We thank the colleagues of the German Center for Neurodegenerative Diseases (DZNE)-Ulm for
656 helpful comments.
657
658 *Authors' contributions*
659 DB contributed to experimental design and performed the stereotactic injections and processed
660 the samples for imaging and performed the image analysis using the WholeBrain registration.
661 SA wrote the image analysis pipeline and performed the manual parcellation study. HPM and JK
662 performed the analysis of the MRI-DTI dataset. AL contributed to the MRI-DTI dataset. FR and JK

designed the experiments, analyzed the data and wrote the first version of the manuscript. FR, JK, AL, TB and LD contributed to the final version of the manuscript and to the interpretation of the findings. All authors read and approved the final manuscript.

Conflict of interst

The authors declare no financial interest or conflict of interest.

Ethics approval and consent to participate

The animal experiments were approved by the Regierungspräsidium Tübingen under the animal license- number 1390 and by the Ulm University Tierforschungszentrum committee.

The collection of MRI-DTI data from human subjects has been approved by the Ethical Committee of the University of Ulm (reference #19/12)

Availability of data and materials

The datasets used and/or analysed during the current study are available from the corresponding author on reasonable request.

Funding

FR is supported by the Thierry Latran Foundation (projects “Trials” and “Hypothals”), by the Radala Foundation, by the Deutsche Forschungsgemeinschaft (DFG, German Research Foundation)- Project-ID 251293561 – Collaborative Research Center (CRC) 1149 and with the individual grant no. 431995586 (RO-5004/8-1) and no. 443642953 (RO5004/9-1), by the Cellular

and Molecular Mechanisms in Aging (CEMMA) Research Training Group and by BMBF (FKZ 01EW1705A, as member of the ERANET-NEURON consortium “MICRONET”). SA and DB are members of the International Graduate School in Molecular Medicine at Ulm University; DB is part of the Graduate School in Cellular and Molecular Mechanisms in Aging at Ulm University.

References:

1) Hardiman O, Al-Chalabi A, Chio A, et al. Amyotrophic lateral sclerosis [published correction appears in Nat Rev Dis Primers. 2017 Oct 20;3:17085]. *Nat Rev Dis Primers*. 2017;3:17071. Published 2017 Oct 5. doi:10.1038/nrdp.2017.71

2) Dupuis L, Pradat PF, Ludolph AC, Loeffler JP. Energy metabolism in amyotrophic lateral sclerosis. *Lancet Neurol*. 2011;10(1):75-82. doi:10.1016/S1474-4422(10)70224-6

3) Peter RS, Rosenbohm A, Dupuis L, et al. Life course body mass index and risk and prognosis of amyotrophic lateral sclerosis: results from the ALS registry Swabia. *Eur J Epidemiol*. 2017;32(10):901-908. doi:10.1007/s10654-017-0318-z

4) Gallo V, Wark PA, Jenab M, et al. Prediagnostic body fat and risk of death from amyotrophic lateral sclerosis: the EPIC cohort. *Neurology*. 2013;80(9):829-838. doi:10.1212/WNL.0b013e3182840689

5) Dupuis L, Corcia P, Fergani A, et al. Dyslipidemia is a protective factor in amyotrophic lateral sclerosis. *Neurology*. 2008;70(13):1004-1009. doi:10.1212/01.wnl.0000285080.70324.27

6) Dorst J, Kühnlein P, Hendrich C, Kassubek J, Sperfeld AD, Ludolph AC. Patients with elevated triglyceride and cholesterol serum levels have a prolonged survival in amyotrophic lateral sclerosis. *J Neurol*. 2011;258(4):613-617. doi:10.1007/s00415-010-5805-z

7) Lindauer E, Dupuis L, Müller HP, Neumann H, Ludolph AC, Kassubek J. Adipose Tissue Distribution Predicts Survival in Amyotrophic Lateral Sclerosis. *PLoS One*. 2013;8(6):e67783. Published 2013 Jun 27. doi:10.1371/journal.pone.0067783

8) Marin B, Desport JC, Kajeu P, et al. Alteration of nutritional status at diagnosis is a prognostic factor for survival of amyotrophic lateral sclerosis patients. *J Neurol Neurosurg Psychiatry*. 2011;82(6):628-634. doi:10.1136/jnnp.2010.211474

9) Steyn FJ, Ioannides ZA, van Eijk RPA, et al. Hypermetabolism in ALS is associated with greater functional decline and shorter survival. *J Neurol Neurosurg Psychiatry*. 2018;89(10):1016-1023. doi:10.1136/jnnp-2017-317887

10) Jésus P, Fayemendy P, Nicol M, et al. Hypermetabolism is a deleterious prognostic factor in patients with amyotrophic lateral sclerosis. *Eur J Neurol*. 2018;25(1):97-104. doi:10.1111/ene.13468

11) Ahmed RM, Irish M, Piguet O, et al. Amyotrophic lateral sclerosis and frontotemporal dementia: distinct and overlapping changes in eating behaviour and metabolism [published correction appears in Lancet Neurol. 2016 Apr;15(4):352]. *Lancet Neurol*. 2016;15(3):332-342. doi:10.1016/S1474-4422(15)00380-4

12) Desport JC, Torny F, Lacoste M, Preux PM, Couratier P. Hypermetabolism in ALS: correlations with clinical and paraclinical parameters. *Neurodegener Dis*. 2005;2(3-4):202-207. doi:10.1159/000089626

13) Bouteloup C, Desport JC, Clavelou P, et al. Hypermetabolism in ALS patients: an early and persistent phenomenon. *J Neurol*. 2009;256(8):1236-1242. doi:10.1007/s00415-009-5100-z

14) Dupuis L, Oudart H, René F, Gonzalez de Aguilar JL, Loeffler JP. Evidence for defective energy homeostasis in amyotrophic lateral sclerosis: benefit of a high-energy diet in a transgenic mouse model. *Proc Natl Acad Sci U S A*. 2004;101(30):11159-11164. doi:10.1073/pnas.0402026101

15) Ludolph AC, Dorst J, Dreyhaupt J, et al. Effect of High-Caloric Nutrition on Survival in Amyotrophic Lateral Sclerosis. *Ann Neurol*. 2020;87(2):206-216. doi:10.1002/ana.25661

16) González JA, Iordanidou P, Strom M, Adamantidis A, Burdakov D. Awake dynamics and brain-wide direct inputs of hypothalamic MCH and orexin networks. *Nat Commun*. 2016;7:11395. Published 2016 Apr 22. doi:10.1038/ncomms11395

17) Barbier M, Chometton S, Pautrat A, et al. A basal ganglia-like cortical-amygdalar-hypothalamic network mediates feeding behavior. *Proc Natl Acad Sci U S A*. 2020;117(27):15967-15976. doi:10.1073/pnas.2004914117

18) Barbier M, González JA, Houdayer C, Burdakov D, Risold PY, Croizier S. Projections from the dorsomedial division of the bed nucleus of the stria terminalis to hypothalamic nuclei in the mouse [published online ahead of print, 2020 Jul 17]. *J Comp Neurol*. 2020;10.1002/cne.24988. doi:10.1002/cne.24988

19) Murata K, Kinoshita T, Fukazawa Y, et al. GABAergic neurons in the olfactory cortex projecting to the lateral hypothalamus in mice. *Sci Rep*. 2019;9(1):7132. Published 2019 May 9. doi:10.1038/s41598-019-43580-1

20) Berthoud HR. Multiple neural systems controlling food intake and body weight. *Neurosci Biobehav Rev*. 2002;26(4):393-428. doi:10.1016/s0149-7634(02)00014-3

21) Commisso B, Ding L, Varadi K, et al. Stage-dependent remodeling of projections to motor cortex in ALS mouse model revealed by a new variant retrograde-AAV9. *Elife*. 2018;7:e36892. Published 2018 Aug 23. doi:10.7554/eLife.36892

22) Agosta F, Canu E, Valsasina P, et al. Divergent brain network connectivity in amyotrophic lateral sclerosis. *Neurobiol Aging*. 2013;34(2):419-427. doi:10.1016/j.neurobiolaging.2012.04.015

23) Schulthess I, Gorges M, Müller HP, et al. Functional connectivity changes resemble patterns of pTDP-43 pathology in amyotrophic lateral sclerosis. *Sci Rep*. 2016;6:38391. Published 2016 Dec 8. doi:10.1038/srep38391

24) Heimrath J, Gorges M, Kassubek J, et al. Additional resources and the default mode network: Evidence of increased connectivity and decreased white matter integrity in amyotrophic lateral sclerosis. *Amyotroph Lateral Scler Frontotemporal Degener*. 2014;15(7-8):537-545. doi:10.3109/21678421.2014.911914

25) Dukic S, McMackin R, Buxo T, et al. Patterned functional network disruption in amyotrophic lateral sclerosis. *Hum Brain Mapp*. 2019;40(16):4827-4842. doi:10.1002/hbm.24740

26) Braak H, Brettschneider J, Ludolph AC, Lee VM, Trojanowski JQ, Del Tredici K. Amyotrophic lateral sclerosis--a model of corticofugal axonal spread. *Nat Rev Neurol*. 2013;9(12):708-714. doi:10.1038/nrneurol.2013.221

27) Brettschneider J, Del Tredici K, Toledo JB, et al. Stages of pTDP-43 pathology in amyotrophic lateral sclerosis. *Ann Neurol*. 2013;74(1):20-38. doi:10.1002/ana.23937

28) Scekic-Zahirovic J, Sendscheid O, El Oussini H, et al. Toxic gain of function from mutant FUS protein is crucial to trigger cell autonomous motor neuron loss. *EMBO J*. 2016;35(10):1077-1097. doi:10.15252/embj.201592559

29) Ouali Alami N, Schurr C, Olde Heuvel F, et al. NF-κB activation in astrocytes drives a stage-specific beneficial neuroimmunological response in ALS. *EMBO J*. 2018;37(16):e98697. doi:10.15252/embj.201798697

30) Tervo DG, Hwang BY, Viswanathan S, et al. A Designer AAV Variant Permits Efficient Retrograde Access to Projection Neurons. *Neuron*. 2016;92(2):372-382. doi:10.1016/j.neuron.2016.09.021

31) Madisen L, Garner AR, Shimaoka D, et al. Transgenic mice for intersectional targeting of neural sensors and effectors with high specificity and performance. *Neuron*. 2015;85(5):942-958. doi:10.1016/j.neuron.2015.02.022

32) Paxinos G, Franklin KBJ. The mouse brain in stereotaxic coordinates, second edition. (*ACADEMIC PRESS*, 2001), ISBN: 0-12-547636-1

33) Schindelin J, Arganda-Carreras I, Frise E, et al. Fiji: an open-source platform for biological-image analysis. *Nat Methods*. 2012;9(7):676-682. Published 2012 Jun 28. doi:10.1038/nmeth.2019

34) Fürth D, Vaissière T, Tzortzi O, et al. An interactive framework for whole-brain maps at cellular resolution [published correction appears in Nat Neurosci. 2017 Dec 18;:]. *Nat Neurosci*. 2018;21(1):139-149. doi:10.1038/s41593-017-0027-7

35) Lein ES, Hawrylycz MJ, Ao N, et al. Genome-wide atlas of gene expression in the adult mouse brain. *Nature*. 2007;445(7124):168-176. doi:10.1038/nature05453

36) Berg S, Kutra D, Kroeger T, et al. ilastik: interactive machine learning for (bio)image analysis. *Nat Methods*. 2019;16(12):1226-1232. doi:10.1038/s41592-019-0582-9

37) Fiaschi L, Koethe U, Nair R, Hamprecht FA. Learning to count with regression forest and structured labels. *Proceedings of the 21st International Conference on Pattern Recognition (ICPR2012)*, Tsukuba, 2012;2685-2688.

38) Sahoo P, Wilkins C, Yeager J. Threshold selection using Renyi's entropy. Pattern Recognition. 1997;30(1):71-84. doi:10.1016/S0031-3203(96)00065-9

39) Kassubek J, Müller HP, Del Tredici K, et al. Imaging the pathoanatomy of amyotrophic lateral sclerosis in vivo: targeting a propagation-based biological marker. *J Neurol Neurosurg Psychiatry*. 2018;89(4):374-381. doi:10.1136/jnnp-2017-316365

40) Müller HP, Unrath A, Ludolph AC, Kassubek J. Preservation of diffusion tensor properties during spatial normalization by use of tensor imaging and fibre tracking on a normal brain database. *Phys Med Biol*. 2007;52(6):N99-N109. doi:10.1088/0031-9155/52/6/N01

41) Müller HP, Del Tredici K, Lulé D, et al. In vivo histopathological staging in C9orf72-associated ALS: A tract of interest DTI study. *Neuroimage Clin*. 2020;27:102298. doi:10.1016/j.nicl.2020.102298

42) Müller HP, Unrath A, Sperfeld AD, Ludolph AC, Riecker A, Kassubek J. Diffusion tensor imaging and tractwise fractional anisotropy statistics: quantitative analysis in white matter pathology. *Biomed Eng Online*. 2007;6:42. Published 2007 Nov 9. doi:10.1186/1475-925X-6-42

43) Petrik MS, Wilson JM, Grant SC, et al. Magnetic resonance microscopy and immunohistochemistry of the CNS of the mutant SOD murine model of ALS reveals widespread neural deficits. *Neuromolecular Med*. 2007;9(3):216-229. doi:10.1007/s12017-007-8002-1

44) Pickles S, Destroismaisons L, Peyrard SL, et al. Mitochondrial damage revealed by immunoselection for ALS-linked misfolded SOD1. *Hum Mol Genet*. 2013;22(19):3947-3959. doi:10.1093/hmg/ddt249

45) Scekic-Zahirovic J, Oussini HE, Mersmann S, et al. Motor neuron intrinsic and extrinsic mechanisms contribute to the pathogenesis of FUS-associated amyotrophic lateral sclerosis. *Acta Neuropathol*. 2017;133(6):887-906. doi:10.1007/s00401-017-1687-9

46) Mariosa D, Beard JD, Umbach DM, et al. Body Mass Index and Amyotrophic Lateral Sclerosis: A Study of US Military Veterans. *Am J Epidemiol*. 2017;185(5):362-371. doi:10.1093/aje/kww140

47) Vercruysse P, Vieau D, Blum D, Petersén Å, Dupuis L. Hypothalamic Alterations in Neurodegenerative Diseases and Their Relation to Abnormal Energy Metabolism. *Front Mol Neurosci*. 2018;11:2. Published 2018 Jan 19. doi:10.3389/fnmol.2018.00002

48) Gorges M, Vercruysse P, Müller HP, et al. Hypothalamic atrophy is related to body mass index and age at onset in amyotrophic lateral sclerosis. *J Neurol Neurosurg Psychiatry*. 2017;88(12):1033-1041. doi:10.1136/jnnp-2017-315795

49) Cykowski MD, Takei H, Schulz PE, Appel SH, Powell SZ. TDP-43 pathology in the basal forebrain and hypothalamus of patients with amyotrophic lateral sclerosis. *Acta Neuropathol Commun*. 2014;2:171. Published 2014 Dec 24. doi:10.1186/s40478-014-0171-1

50) Vercruysse P, Sinniger J, El Oussini H, et al. Alterations in the hypothalamic melanocortin pathway in amyotrophic lateral sclerosis. *Brain*. 2016;139(Pt 4):1106-1122. doi:10.1093/brain/aww004

51) Meng D, Li HQ, Deisseroth K, Leutgeb S, Spitzer NC. Neuronal activity regulates neurotransmitter switching in the adult brain following light-induced stress. Proc Natl Acad Sci U S A. 2018 May 15;115(20):5064-5071.

52) Floyd NS, Price JL, Ferry AT, Keay KA, Bandler R. Orbitomedial prefrontal cortical projections to hypothalamus in the rat. *J Comp Neurol*. 2001;432(3):307-328. doi:10.1002/cne.1105

53) Hoover WB, Vertes RP. Projections of the medial orbital and ventral orbital cortex in the rat. *J Comp Neurol*. 2011;519(18):3766-3801. doi:10.1002/cne.22733

54) Roberts AC, Tomic DL, Parkinson CH, et al. Forebrain connectivity of the prefrontal cortex in the marmoset monkey (Callithrix jacchus): an anterograde and retrograde tract-tracing study. *J Comp Neurol*. 2007;502(1):86-112. doi:10.1002/cne.21300

55) Ongür D, An X, Price JL. Prefrontal cortical projections to the hypothalamus in macaque monkeys. *J Comp Neurol*. 1998;401(4):480-505.

56) Price JL. Definition of the orbital cortex in relation to specific connections with limbic and visceral structures and other cortical regions. *Ann N Y Acad Sci*. 2007;1121:54-71. doi:10.1196/annals.1401.008

57) Alexander AL, Lee JE, Lazar M, Field AS. Diffusion tensor imaging of the brain. *Neurotherapeutics*. 2007;4(3):316-329. doi:10.1016/j.nurt.2007.05.011

58) Kobayashi M. Macroscopic connection of rat insular cortex: anatomical bases underlying its physiological functions. *Int Rev Neurobiol*. 2011;97:285-303. doi:10.1016/B978-0-12-385198-7.00011-4

59) Izquierdo A. Functional Heterogeneity within Rat Orbitofrontal Cortex in Reward Learning and Decision Making. *J Neurosci*. 2017;37(44):10529-10540. doi:10.1523/JNEUROSCI.1678-17.2017

60) Rolls ET. The functions of the orbitofrontal cortex. *Brain Cogn*. 2004;55(1):11-29. doi:10.1016/S0278-2626(03)00277-X

61) Seabrook LT, Borgland SL. The orbitofrontal cortex, food intake and obesity. *J Psychiatry Neurosci*. 2020;45(5):304-312. doi:10.1503/jpn.190163

62) Schur EA, Kleinhans NM, Goldberg J, Buchwald D, Schwartz MW, Maravilla K. Activation in brain energy regulation and reward centers by food cues varies with choice of visual stimulus. *Int J Obes (Lond)*. 2009;33(6):653-661. doi:10.1038/ijo.2009.56

63) Suzuki S, Cross L, O'Doherty JP. Elucidating the underlying components of food valuation in the human orbitofrontal cortex. *Nat Neurosci*. 2017;20(12):1780-1786. doi:10.1038/s41593-017-0008-x

939 64) Raji CA, Ho AJ, Parikshak NN, et al. Brain structure and obesity. *Hum Brain Mapp*.
940 2010;31(3):353-364. doi:10.1002/hbm.20870
941
942 65) Walther K, Birdsill AC, Glisky EL, Ryan L. Structural brain differences and cognitive
943 functioning related to body mass index in older females. *Hum Brain Mapp*.
944 2010;31(7):1052-1064. doi:10.1002/hbm.20916
945
946 66) Alkan A, Sahin I, Keskin L, et al. Diffusion-weighted imaging features of brain in obesity.
947 *Magn Reson Imaging*. 2008;26(4):446-450. doi:10.1016/j.mri.2007.10.004
948
949 67) Burg T, Bichara C, Scekic-Zahirovic J, et al. Absence of Subcerebral Projection Neurons Is
950 Beneficial in a Mouse Model of Amyotrophic Lateral Sclerosis [published online ahead of
951 print, 2020 Jun 26]. *Ann Neurol*. 2020;10.1002/ana.25833. doi:10.1002/ana.25833
952

953

954 **Supplementary:**

955 **Supplementary *Table 1***: Anatomical landmarks used for mapping the brain section from
956 anterior to posterior. The following structures provided distinctive optical characteristics for
957 mapping: AOB = Accessory olfactory bulb; DP = Dorsal peduncular area; fa = corpus callosum,
958 anterior forceps; ccg = genu of corpus callosum; aco = anterior commissure, olfactory limb; act =
959 anterior commissure, temporal limb; SCH = Suprachiasmatic nucleus; NLOT = Nucleus of the
960 lateral olfactory tract; ME = Median eminence; opt = optic tract; int = internal capsule; DG =
961 Dentate gyrus; CA3so = Field CA3, stratum oriens; MM = Medial mammillary nucleus.
962

Coordinate from bregma	Anatomical landmark	Section in Allen´s brain atlas
2,6	first section without AOB	27
2,2	section before beginning of DP	32
2,1	first section with DP	33
1,6	shape of fa	38
1,5	shape of fa	39
1,4	shape of fa	40
1,2	shape of fa	42
1,1	shape of fa	43
1	shape of ccg	44
0,2	shape of aco	52
0,1	shape of aco	53
0	shape of aco and act	54
-0,3	first section with SCH last section without NLOT	57
-1	shape of opt last section with NLOT	64
-1,4	first section with ME shape of otp and int	69
-2,2	first section without ME first section with ventral DG	76
-2,5	Expansion of CA3so	79
-3,1	last section with MM	85

963
964

Supplementary Table 2: List of structures of the brain projecting to LHA. For each structure, the absolute number of neurons projecting to LHA is reported as mean ± SD and independently for ipsi- and contralateral hemispheres.

	Ipsilateral raw data	**Contralateral raw data**	**Ipsilateral normalized**	**Contralateral normalized**
A13	85.6, ±45.9	10.4, ±6.6	58.5, ±28.2	7.1, ±3.8
AAA	297.6, ±230.0	18.8, ±7.2	225.3, ±128.1	16.3, ±7.4
ACA	2686.2, ±1373.5	897.0, ±468.9	1826.0, ±538.9	599.4, ±232.6
ACB	565.4, ±375.1	9.4, ±10.1	411.8, ±173.1	7.9, ±6.9
ADP	64.4, ±27.3	16.6, ±8.6	48.3, ±10.8	12.5, ±4.1
AHN	1174.0, ±1241.1	111.4, ±91.1	909.7, ±1146.0	84.7, ±77.7
AI	1437.8, ±1365.3	197.0, ±177.6	935.9, ±622.2	117.2, ±82.2
AON	92.2, ±90.1	6.2, ±4.4	64.6, ±41.4	4.1, ±1.6
APN	54.2, ±43.3	5.4, ±1.7	35.4, ±19.1	5.7, ±4.8
AUD	228.6, ±246.6	62.2, ±48.6	138.4, ±129.3	38.0, ±27.4
AVP	207.8, ±99.8	71.6, ±36.0	143.2, ±41.5	49.3, ±22.1
AVPV	242.0, ±43.6	71.2, ±31.5	216.0, ±99.8	70.5, ±57.7
BLA	1263.0, ±670.4	79.6, ±56.3	920.2, ±278.5	52.6, ±28.0
BMA	1405.0, ±744.5	110.4, ±67.5	1009.6, ±381.6	77.4, ±37.9
BST	2108.8, ±774.0	275.6, ±165.1	1613.9, ±236.4	188.0, ±82.2
CEA	440.4, ±315.9	14.4, ±6.8	292.6, ±129.9	12.6, ±7.0
CLA	20.0, ±11.5	4.4, ±2.2	14.8, ±4.9	3.8, ±2.1
CM	132.8, ±65.5	49.2, ±18.7	97.1, ±40.2	37.5, ±7.1
COA	730.4, ±377.3	39.2, ±31.1	539.2, ±179.2	25.4, ±17
CP	814.4, ±499.4	34.8, ±21.2	581.7, ±185.8	23.0, ±7.0
DMH	1510.0, ±729.1	233.8, ±115.7	1039.7, ±290.7	160.3, ±50
DP	618.4, ±249.1	192.2, ±128.9	535.8, ±289.4	131.5, ±54.3
ECT	255.8, ±139.4	79.0, ±50.1	172.5, ±48.9	50.5, ±26.3
ENTI	144.8, ±96.2	28.6, ±18.1	98.2, ±46.0	18.1, ±10.3
EP	252.0, ±241.5	9.4, ±8.1	175.9, ±109.7	5.8, ±4.8
FS	59.8, ±45.7	1.0, ±0.9	48.2, ±31.9	0.7, ±0.7
GP	133.8, ±83.9	9.8, ±10.7	90.2, ±27.0	6.0, ±5.3
GU	503.2, ±399.3	77.0, ±63.8	343.9, ±186.6	49.7, ±28.3
IA	127.4, ±90.9	8.0, ±5.8	92.8, ±70.4	6.5, ±5.0
ILA	2627.2, ±896.1	1192.2, ±548.6	2089.0, ±476.3	834.9, ±188.3
IMD	145.8, ±74.4	55.8, ±29.8	103.6, ±34.6	37.5, ±11.9
LH	188.4, ±99.4	32.6, ±17.2	127.9, ±41.1	21.8, ±9.0
LHA	Injection	845.8, ±509.0	Injection	573.8, ±167.2
LPO	1251.6, ±447.7	173.2, ±113.4	1000.5, ±271.0	120.5, ±51.3
LS	1453.4, ±583.2	179.6, ±78.9	1169.3, ±436.5	127.3, ±23.3
MA	139.6, ±177.3	5.8, ±4.1	97.8, ±90.1	6.0, ±6.1

MEA	712.8, ±691.0	72.4, ±103.5	499.2, ±437.3	46.6, ±66.8
MEPO	252.8, ±96.0	204.6, ±71.7	207.2, ±71.9	169.9, ±57.2
MM	126.0, ±105.5	55.2, ±49.2	86.8, ±54.7	36.4, ±29.1
MOp	1006.4, ±1321.7	71.6, ±74.0	576.5, ±705.8	40.4, ±38.2
MOs	2292.6, ±2310.5	273.6, ±224.4	1391.5, ±1146.2	168.8, ±103.4
MPN	701.2, ±246.6	177.2, ±104.2	551.6, ±124.7	121.4, ±56.4
MPO	1752.4, ±543.1	436.4, ±213.4	1384.5, ±259.7	306.7, ±83.4
MS	323.0, ±157.8	58.4, ±29.3	240.5, ±56.7	47.0, ±16.7
NDB	288.2, ±281.3	34.4, ±24.5	202.7, ±126.0	24.7, ±20.6
NLOT	74.0, ±40.3	8.0, ±5.4	55.9, ±20.7	5.5, ±3.1
OLF	125.4, ±76.6	19.0, ±11.4	97.4, ±39.3	13.5, ±4.9
ORBl	306.6, ±425.5	41.8, ±68.5	168.7, ±213.7	22.7, ±34.6
ORBm	515.4, ±261.3	142.6, ±120.6	421.2, ±183.3	104.2, ±53.7
ORBvl	184.8, ±193.9	31.4, ±42.7	110.2, ±90.7	18.6, ±20.7
OT	58.4, ±74.6	1.8, ±1.7	37.9, ±35.2	1.5, ±1.0
OV	28.2, ±9.0	17.2, ±4.2	24.9, ±12.4	16.2, ±9.8
PA	398.4, ±541.0	156.2, ±271.9	252.9, ±347.2	99.8, ±175.5
PAA	31.2, ±11.4	2.6, ±0.8	25.3, ±7.4	2.5, ±1.5
PD	17.8, ±7.0	3.6, ±3.8	14.7, ±5.9	2.6, ±2.3
PERI	235.0, ±141.4	60.8, ±34.0	156.4, ±61.6	39.9, ±15.5
PH	1304.0, ±428.6	662.0, ±209.6	1043.6, ±248.9	528.6, ±123.8
PIR	667.0, ±677.1	27.0, ±12.9	444.4, ±302.3	20.2, ±6.7
PL	1576.0, ±554.1	653.6, ±330.0	1239.8, ±254.5	466.9, ±93.6
PS	33.2, ±20.0	2.8, ±2.5	22.2, ±6.3	1.8, ±1.5
PST	37.0, ±26.9	4.0, ±4.6	41.3, ±47.5	2.9, ±2.5
PSTN	160.2, ±59.7	16.6, ±12.9	168.5, ±158.2	11.4, ±5.6
PTL	199.4, ±198.2	17.0, ±11.1	121.9, ±104.4	11.2, ±5.0
PV	239.8, ±164.1	46.2, ±27.2	171.9, ±111.7	34.1, ±14.2
PVH	449.2, ±210.4	72.4, ±46.7	339.2, ±164.4	50.9, ±33.3
PVT	960.4, ±475.5	332.4, ±231.1	686.5, ±334.9	242.4, ±193.1
RE	461.0, ±379.7	176.4, ±122.5	356.0, ±347.2	134.9, ±109.3
RSP	331.8, ±297.9	47.6, ±32.1	198.7, ±152.4	30.7, ±15.4
SF	57.8, ±32.7	13.6, ±6.0	41.9, ±21.1	9.7, ±3.6
SI	1278.0, ±723.9	71.8, ±65.0	982.8, ±364.2	46.3, ±28.1
SS	700.6, ±860.7	57.4, ±49.5	407.5, ±454	40.5, ±25.0
STN	124.4, ±78.1	20.0, ±11.8	116.4, ±96.7	13.2, ±5.1
SUM	475.2, ±235.5	211.4, ±145.1	370.8, ±110.8	144.5, ±54.0
TEa	205.6, ±122.0	78.6, ±58.0	136.7, ±45.9	49.3, ±29.6
TRS	27.8, ±18.0	20.4, ±19.1	24.1, ±16.7	14.6, ±11.3
TT	929.4, ±512.0	214.6, ±194.3	802.0, ±531.2	131.0, ±95.0
TU	531.4, ±445.1	60.8, ±36.4	353.3, ±263.6	41.7, ±18.4
VIS	68.4, ±49.9	5.0, ±4.1	42.7, ±26.3	3.6, ±3.7

VISC	138.6, ±109.1	22.0, ±21.0	86.0, ±49.0	14.3, ±9.3
VLPO	57.4, ±30.1	17.8, ±15.3	40.3, ±11.4	11.3, ±9.3
VM	821.2, ±745.3	84.8, ±34.6	523.4, ±351.8	63.8, ±20.3
VMH	1462.6, ±799.9	187.4, ±149.2	1004.7, ±629.3	137.7, ±133.4
VP	163.2, ±158.4	28.0, ±12.4	110.7, ±75.8	21.4, ±5.6
ZI	1829.0, ±912.2	263.0, ±107.7	1374.4, ±334.2	194.9, ±34.7

Supplementary Figure 1-9 are provided in a separate PDF

Supplementary Fig. 1: Altered cortico-hypothalamic projection pattern in mSOD1 mice at P95, absolute counts ipsilateral. A: Sum of neurons projecting from selected 28 areas. Significantly increased projections from ipsilateral hemisphere in mSOD mice to LHA (p=0.02; n=3). B: Quantification of the absolute number of neurons projecting to LHA from 28 brain structures in WT and mSOD1. A significant increase in projections from ACA (p<0.0001), ILA (p=0.009), ORBl/vl+AI (p<0.0001), Tenia Tecta (TT; p=0.0365), secondary Motor Cortex (MOs, p<0.0001) and Piriform cortex (PIR; p=0.0005). C: Representative *WholeBrain* ipsilateral side view reconstructions of neurons projecting to LHA in WT and mSOD1 mice. Expansion of projections from MOs are visible (arrows). D: Representative *WholeBrain* cortical top view reconstructions of neurons projecting to LHA in WT and mSOD1 mice. Expansion of projections from MOs are visible (arrows). Bars show mean ± SD. *p < 0.05, **p < 0.01, ***p < 0.001, ****p< 0.0001.

Supplementary Fig. 2: Altered cortico-hypothalamic projection pattern in mSOD1 mice at P95, contralateral hemisphere. A: Sum of neurons projecting from selected 28 areas. No difference is detected in the summarized number of neurons projecting to LHA in WT and mSOD1 from the contralateral hemisphere (n=3). B: Quantification of the absolute number of neurons projecting to LHA from 28 brain structures in WT and mSOD1. A significant increase in projections from ACA (p=0.0008), PL+ORBm and ILA (both p<0.0001) is detected. C: No difference is detected in the quantification of the normalized number of neurons projecting to LHA from 28 brain structures in WT and mSOD1. Bars show mean ± SD. *p < 0.05, **p < 0.01, ***p < 0.001, ****p< 0.0001.

Supplementary Fig. 3: Primary motor cortex and somatosensory cortex atrophy in P95 mSOD mice. Volumetric comparison of 28 areas in WT and mSOD. Significant atrophy was detected in MOp and SS. Bars show mean ± SD. *p < 0.05, **p < 0.01, ***p < 0.001, ****p< 0.0001.

Supplementary Fig. 4: Altered cortico-hypothalamic projection pattern in manual registered mSOD1 mice at P95, ipsilateral. A: Left: representative injection sites in LHA for WT and mSOD1 mice. White outlines represent LHA boundaries. Middle and right: Representative frontal brain sections of WT and mSOD1 mice depicting projections from ORBl/vl+AI (significantly increased, arrow), PL+ORBm, ILA, ACA, MOs and MOp to LHA. B: Sum of neurons projecting from selected 28 areas. No difference is detected in the summarized number of neurons projecting to LHA in WT and mSOD1 from the ipsilateral hemisphere (n=3). C: Quantification of the absolute number of neurons projecting to LHA from 28 brain structures in WT and mSOD1. A significant increase

in projections from ORBl/vl+AI (p=0.035) is detected. D: Quantification of the normalized number of neurons projecting to LHA from 28 brain structures in WT and mSOD1. A significant increase in projections from ILA (p=0.001) , ORBl/vl+AI (p<0.0001) and PIR (p<0.0001) is detected. Bars show mean ± SD. Scalebars 1 mm. *p < 0.05, **p < 0.01, ***p < 0.001, ****p< 0.0001.

Supplementary Fig. 5: Altered projection pattern in manual registered mSOD1 mice at P95, contralateral. A: Sum of neurons projecting from selected 28 areas. No difference is detected in the summarized number of neurons projecting to LHA in WT and mSOD1 from the contralateral hemisphere (n=3). B: No difference is detected in the quantification of the absolute number of neurons projecting to LHA from 28 brain structures in WT and mSOD1. C: Quantification of the normalized number of neurons projecting to LHA from 28 brain structures in WT and mSOD1. A significant increase in projections from PL+ORBm (p<0.0001) is detected. Bars show mean ± SD. *p < 0.05, **p < 0.01, ***p < 0.001, ****p< 0.0001.

Supplementary Fig. 6: Unaltered cortico-hypothalamic projection pattern in mSOD1 mice at P25, ipsilateral. A: Left: representative injection sites in LHA for WT and mSOD1 mice. White outlines represent LHA boundaries. Middle and right: Representative frontal brain sections of WT and mSOD1 mice depicting a similar pattern of neurons. B: Sum of neurons projecting from selected 28 areas. No difference is detected in the summarized number of neurons projecting to LHA in WT and mSOD1 from the ipsilateral hemisphere (n=3). C: No difference is detected in the quantification of the absolute number of neurons projecting to LHA from 28 brain structures in WT and mSOD1. D: No difference is detected in the quantification of the normalized number of neurons projecting to LHA from 28 brain structures in WT and mSOD1. Bars show mean ± SD. Scalebars 1 mm.

Supplementary Fig. 7: Unaltered cortico-hypothalamic projection pattern in mSOD1 mice at P25, contralateral hemisphere. A: Sum of neurons projecting from selected 28 areas. No difference is detected in the summarized number of neurons projecting to LHA in WT and mSOD1 from the contralateral hemisphere (n=3). B: Quantification of the absolute number of neurons projecting to LHA from 28 brain structures in WT and mSOD1. A significant increase in projections from ACA (p=0.0078) is detected. C: Quantification of the normalized number of neurons projecting to LHA from 28 brain structures in WT and mSOD1. No difference is detected in the quantification of the number of neurons projecting to LHA from 28 brain structures in WT and mSOD1. D: Representative *WholeBrain* volume reconstructions of neurons projecting to LHA in WT and mSOD1 mice show a similar pattern of projections in MOs (blue), ORBl/vl+AI (yellow) and PL+AI (green). Bars show mean ± SD. *p < 0.05, **p < 0.01, ***p < 0.001, ****p< 0.0001.

Supplementary Fig. 8: Altered cortico-hypothalamic projection pattern in kiFUS mice at P270, absolute counts ipsilateral. A: Sum of neurons projecting from selected 28 areas. No difference is detected in the summarized number of neurons projecting to LHA in WT and kiFUS from the ipsilateral hemisphere (n=4). B: Quantification of the absolute number of neurons projecting to LHA from 28 brain structures in WT and mSOD1. A significant increase in projections from ACA

1051 (p=0.0385) and MOs (p<0.0001) is detected. C: Representative *WholeBrain* ipsilateral side view
1052 reconstructions of neurons projecting to LHA in WT and mSOD1 mice. Decrease of projections
1053 from MOs are visible (arrows). D: Representative *WholeBrain* cortical top view reconstructions
1054 of neurons projecting to LHA in WT and mSOD1 mice. Decrease of projections from MOs are
1055 visible (arrows). Bars show mean ± SD. *$p < 0.05$, **$p < 0.01$, ***$p < 0.001$, ****$p < 0.0001$.
1056
1057 ***Supplementary Fig. 9:*** Altered cortico-hypothalamic projection pattern in kiFUS mice at P270,
1058 contralateral hemisphere. A: Sum of neurons projecting from selected 28 areas. No difference is
1059 detected in the summarized number of neurons projecting to LHA in WT and kiFUS from the
1060 contralateral hemisphere (n=3). B: Quantification of the absolute number of neurons projecting
1061 to LHA from 28 brain structures in WT and mSOD1. A significant increase in projections from
1062 ACA (p=0.0121) and ILA (p=0.0474) is detected. C: Quantification of the normalized number of
1063 neurons projecting to LHA from 28 brain structures in WT and kiFUS. A significant decrease in
1064 projections from ACA (p=0.0137) is detected. Bars show mean ± SD. *$p < 0.05$, **$p < 0.01$, ***p
1065 < 0.001, ****$p < 0.0001$.
1066

1067 **Abbreviations**

1068 ABA = Allen brain atlas, version 2011
1069 ACA = Anterior cingulate area
1070 aco = anterior commissure olfactory limb
1071 act = anterior commissure temporal limb
1072 AI = Agranular insular area
1073 ALS = Amyotrophic lateral sclerosis
1074 ALS-FRS-R = ALS functional rating scale revised
1075 AOB = Accessory olfactory bulb
1076 AP = Anteroposterior
1077 AUD = Auditory areas
1078 BLA = Basolateral amygdalar nucleus
1079 BMA = Basolateral amygdalar nucleus
1080 BSA = Bovine serum albumin
1081 CA3so = Field CA3 stratum oriens
1082 ccg = genu of corpus callosum
1083 CLA = Claustrum
1084 COA = Cortical amygdalar area
1085 DG = Dentate gyrus
1086 DP = Dorsal peduncular area
1087 DPBS = Dulbecco's phosphate buffered saline
1088 DTI = Diffusion-tensor-imaging
1089 DV = Dorsoventral
1090 EP = Endopiriform nucleus
1091 fa = corpus callosum anterior forceps
1092 FA = Fractional anisotropy

1093 FUS = B6.FUS$^{\Delta NLS/+}$
1094 HSB = Hue-saturation-brightness color model
1095 GU = Gustatory areas
1096 HY = Hypothalamus
1097 ILA = Infralimbic area
1098 int = internal capsule
1099 kiFUS = FUS^{-}/ZsGreen$^{+/-}$
1100 LA = Lateral amygdalar nucleus
1101 LHA = Lateral hypothalamic area
1102 ME = Median eminence
1103 ML = Mediolateral
1104 MM = Medial mammillary nucleus
1105 MOp = Primary motor area
1106 MOs = Secondary motor area
1107 MRI = Magnetic resonance imaging
1108 mSOD1 = mSOD^{+}/ZsGreen$^{+/-}$
1109 mSOD = B6SJL73 Tg(SOD1*G93A)1Gur/J (high-copy)
1110 NLOT = Nucleus of the lateral olfactory tract
1111 OCT = Optimal cutting temperature compound
1112 opt = optic tract
1113 ORBl/vl = Orbital area, lateral/ventrolateral part
1114 ORBl/vl+ AI = Group of Orbital area, lateral/ventrolateral part and Agranular insular area
1115 ORBm = Orbital area, medial part
1116 OT = Olfactory tubercle
1117 P110 = Post-natal day 110
1118 PA = Posterior amygdalar nucleus
1119 PAA = Piriform-amygdalar area
1120 PBS = Phosphate buffered saline
1121 PFA = Paraformaldehyde
1122 PIR = Piriform area
1123 PL = Prelimbic area
1124 PL+ ORBm = Group of Prelimbic area and Orbital area, medial part
1125 PTL = Posterior parietal association areas
1126 rAAV = recombinant adeno-associated virus
1127 rAAV2-retro = retrograde recombinant adeno-associated virus 2
1128 RAM = Random-access memory
1129 RGB = Red-green-blue color model
1130 Rhinal CTX = Group of Perirhinal area, Ectorhinal area and Entorhinal area, lateral part
1131 ROI = Region of Interest
1132 RSP = Retrosplenial area
1133 rt = room temperature
1134 SCH = Suprachiasmatic nucleus
1135 SS = Somatosensory areas
1136 Tea = Temporal association areas

TFAS = Tractwise fractional anisotropy statistics
tiff = Tagged image file format
TOI = Tract-of-interest
TT = Taenia tecta
VIS = Visual areas
VISC = Visceral area

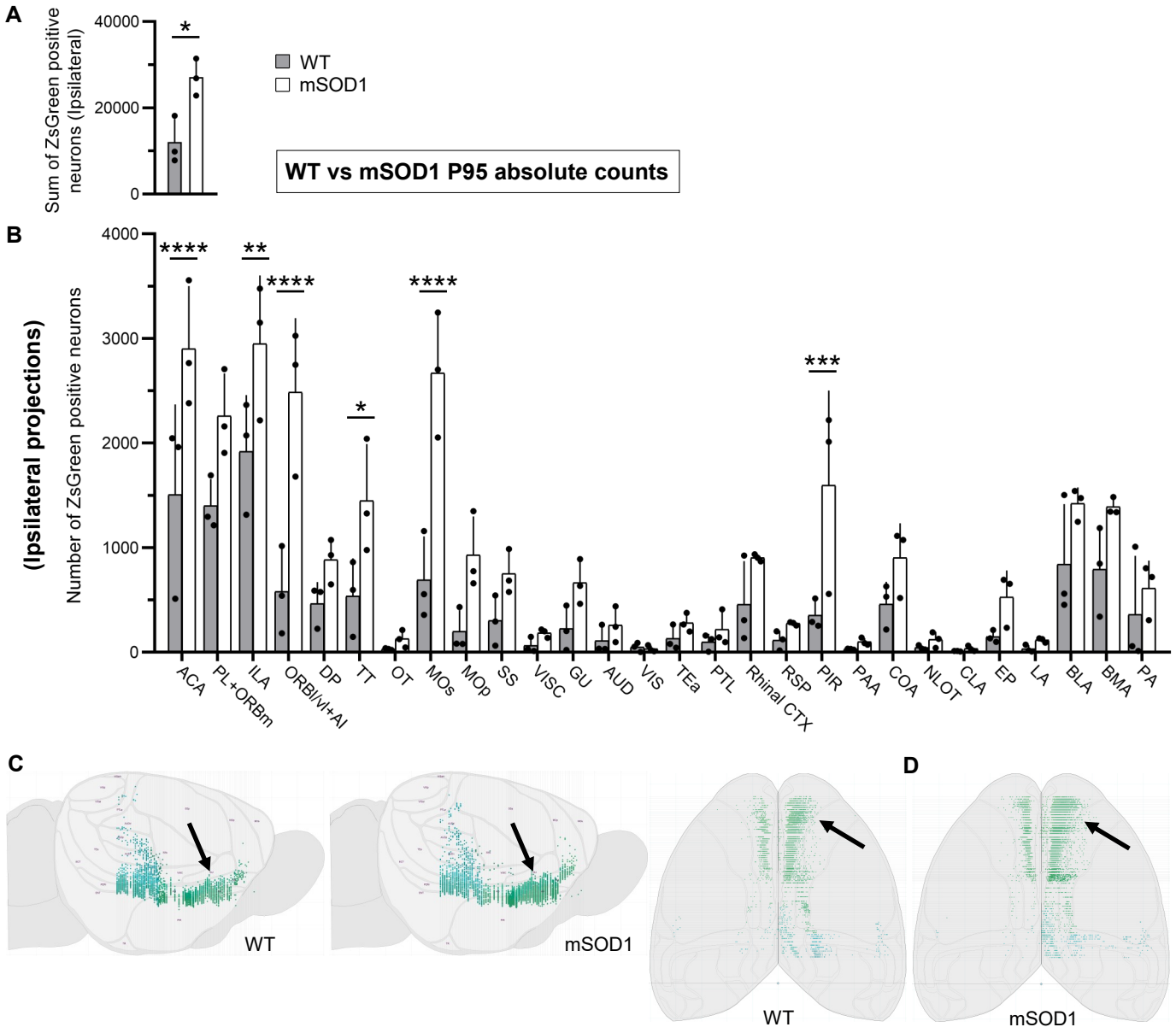
A
Sum of ZsGreen positive neurons (Ipsilateral)
40000
20000
0
*
WT
mSOD1
WT vs mSOD1 P95 absolute counts
B
(Ipsilateral projections)
Number of ZsGreen positive neurons
4000
3000
2000
1000
0
****
**
****
*
****
***
ACA
PL+ORBm
ILA
ORBl/vl+AI
DP
TT
OT
MOs
MOp
SS
VISC
GU
AUD
VIS
TEa
PTL
Rhinal CTX
RSP
PIR
PAA
COA
NLOT
CLA
EP
LA
BLA
BMA
PA
C
WT
mSOD1
D
WT
mSOD1

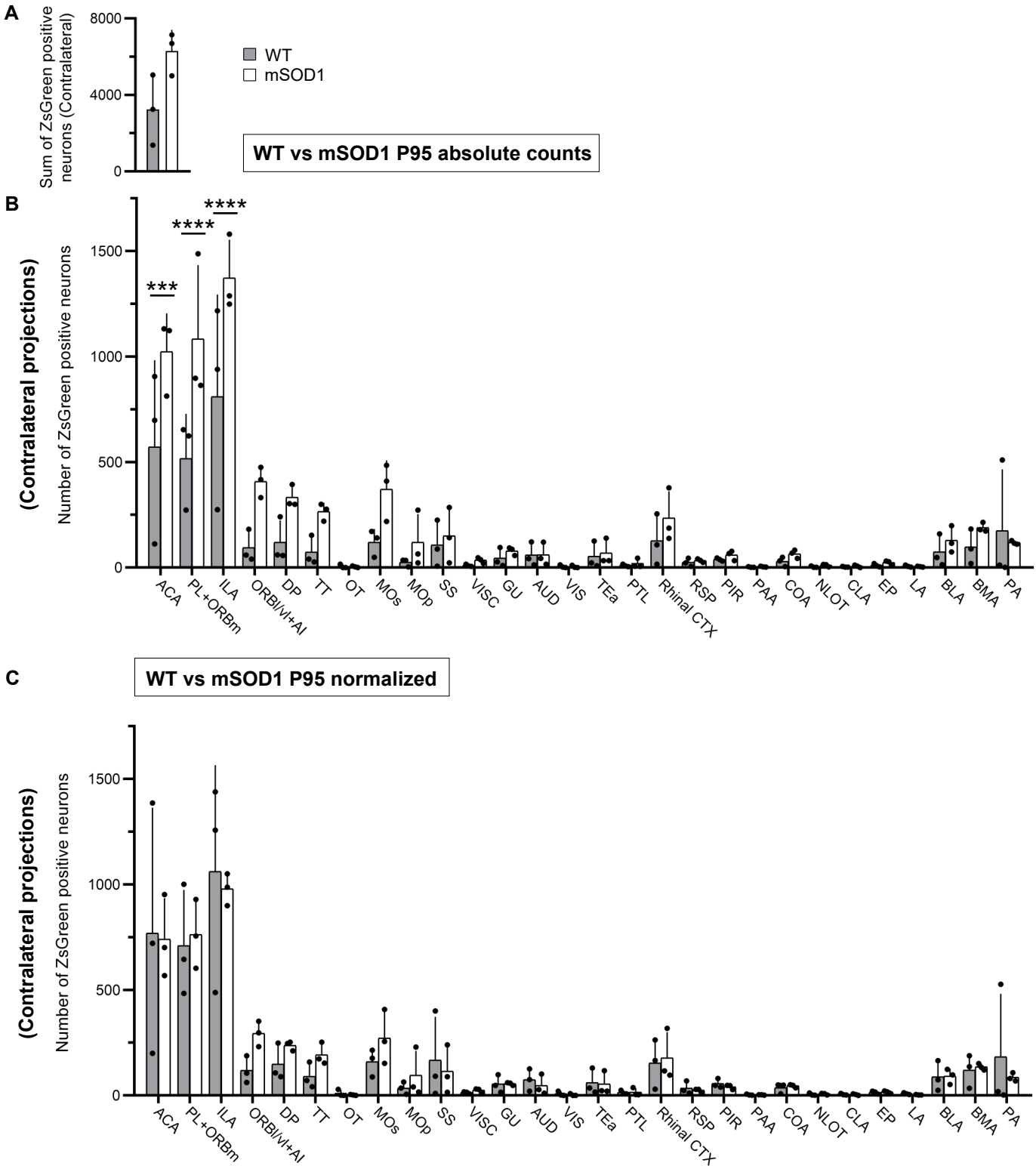
A
Sum of ZsGreen positive neurons (Contralateral)
8000
4000
0
WT
mSOD1
WT vs mSOD1 P95 absolute counts
B
(Contralateral projections)
Number of ZsGreen positive neurons
1500
1000
500
0
***
****
****
ACA
PL+ORBm
ILA
ORBl/vl+AI
DP
TT
OT
MOs
MOp
SS
VISC
GU
AUD
VIS
TEa
PTL
Rhinal CTX
RSP
PIR
PAA
COA
NLOT
CLA
EP
LA
BLA
BMA
PA
C
WT vs mSOD1 P95 normalized
(Contralateral projections)
Number of ZsGreen positive neurons
1500
1000
500
0
ACA
PL+ORBm
ILA
ORBl/vl+AI
DP
TT
OT
MOs
MOp
SS
VISC
GU
AUD
VIS
TEa
PTL
Rhinal CTX
RSP
PIR
PAA
COA
NLOT
CLA
EP
LA
BLA
BMA
PA

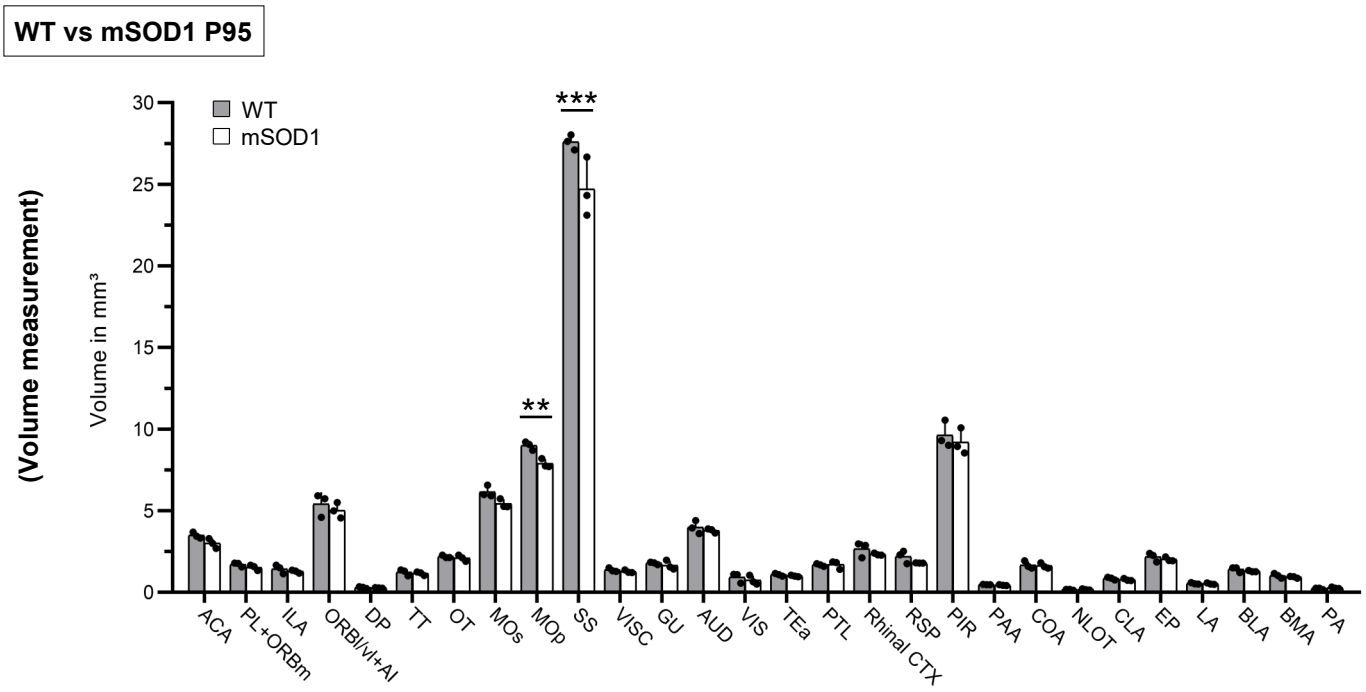
WT vs mSOD1 P95
(Volume measurement)
Volume in mm³
WT
mSOD1
***
**
30
25
20
15
10
5
0
ACA
PL+ORBm
ILA
ORBl/vl+Al
DP
TT
OT
MOs
MOp
SS
VISC
GU
AUD
VIS
TEa
PTL
Rhinal CTX
RSP
PIR
PAA
COA
NLOT
CLA
EP
LA
BLA
BMA
PA

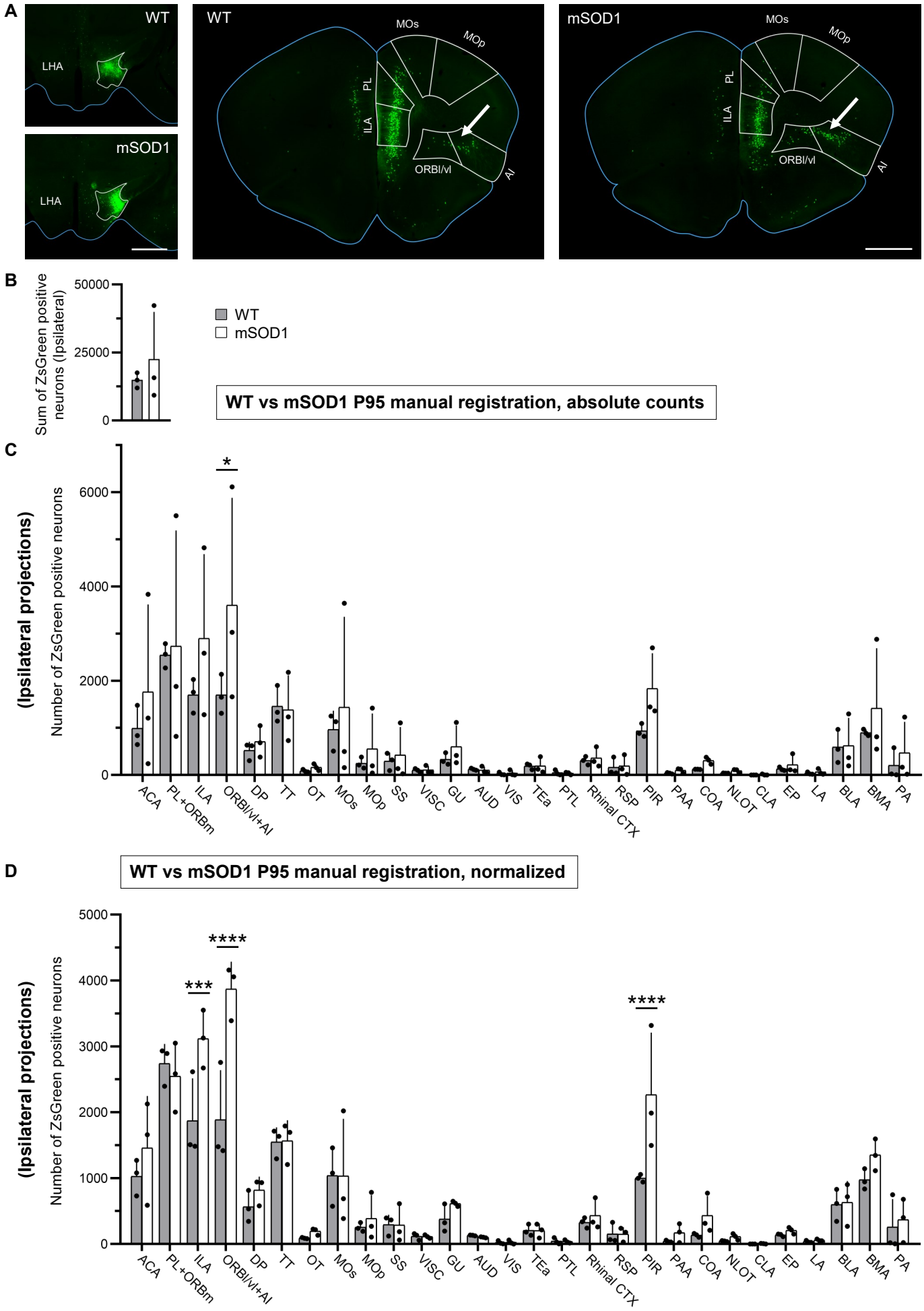
A
WT
LHA
mSOD1
LHA
WT
MOs
MOp
PL
ILA
ORBl/vl
AI
mSOD1
MOs
MOp
PL
ILA
ORBl/vl
AI
B
Sum of ZsGreen positive neurons (Ipsilateral)
50000
25000
0
WT
mSOD1
WT vs mSOD1 P95 manual registration, absolute counts
C
(Ipsilateral projections)
Number of ZsGreen positive neurons
6000
4000
2000
0
*
ACA
PL+ORBm
ILA
ORBl/vl+AI
DP
TT
OT
MOs
MOp
SS
VISC
GU
AUD
VIS
TEa
PTL
Rhinal CTX
RSP
PIR
PAA
COA
NLOT
CLA
EP
LA
BLA
BMA
PA
D
WT vs mSOD1 P95 manual registration, normalized
(Ipsilateral projections)
Number of ZsGreen positive neurons
5000
4000
3000
2000
1000
0
****
***
****
ACA
PL+ORBm
ILA
ORBl/vl+AI
DP
TT
OT
MOs
MOp
SS
VISC
GU
AUD
VIS
TEa
PTL
Rhinal CTX
RSP
PIR
PAA
COA
NLOT
CLA
EP
LA
BLA
BMA
PA

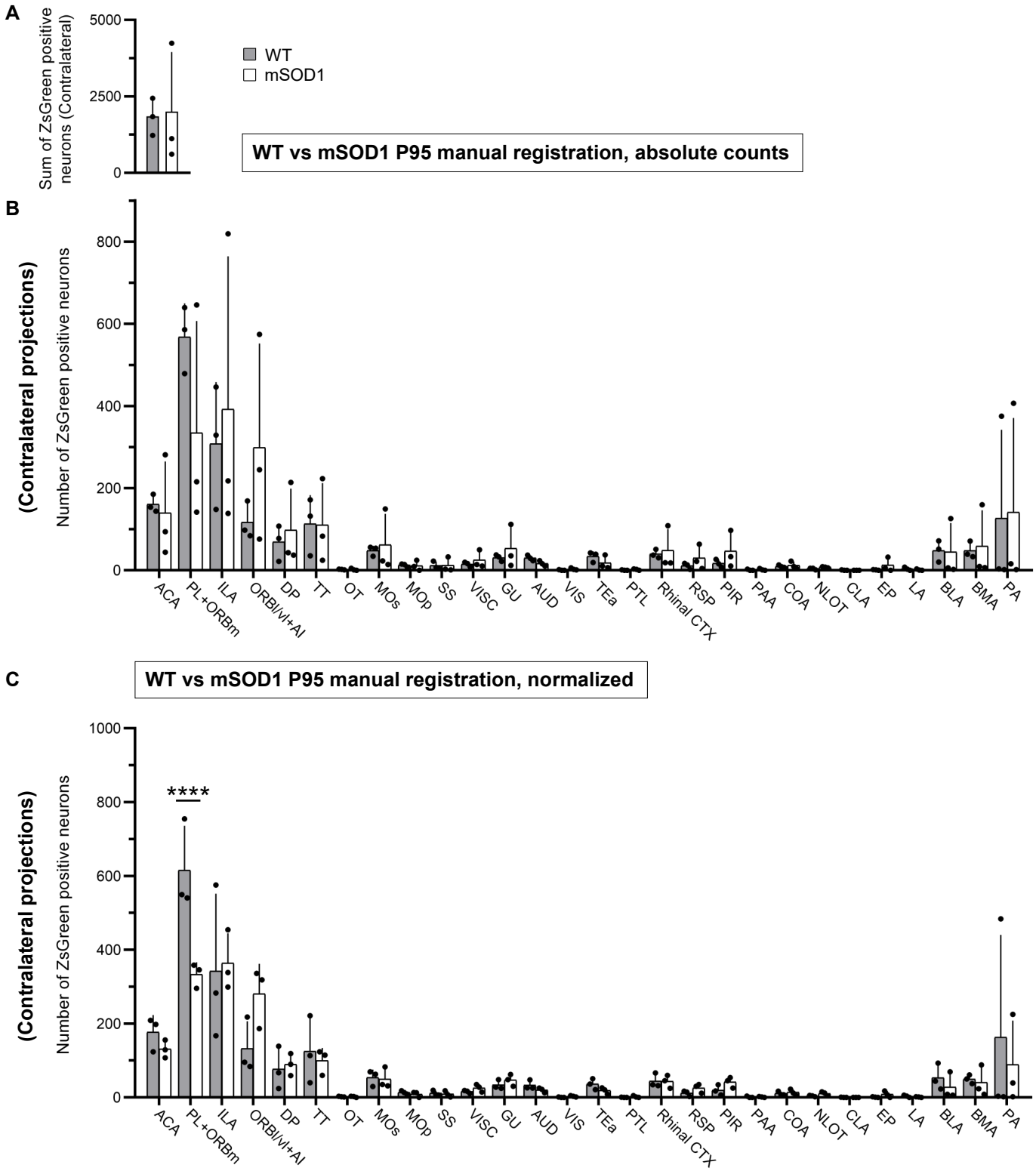
A
Sum of ZsGreen positive neurons (Contralateral)
5000
2500
0
WT
mSOD1
WT vs mSOD1 P95 manual registration, absolute counts
B
(Contralateral projections)
Number of ZsGreen positive neurons
800
600
400
200
0
ACA
PL+ORBm
ILA
ORBl/vl+AI
DP
TT
OT
MOs
MOp
SS
VISC
GU
AUD
VIS
TEa
PTL
Rhinal CTX
RSP
PIR
PAA
COA
NLOT
CLA
EP
LA
BLA
BMA
PA
C
WT vs mSOD1 P95 manual registration, normalized
(Contralateral projections)
Number of ZsGreen positive neurons
1000
800
600
400
200
0
****
ACA
PL+ORBm
ILA
ORBl/vl+AI
DP
TT
OT
MOs
MOp
SS
VISC
GU
AUD
VIS
TEa
PTL
Rhinal CTX
RSP
PIR
PAA
COA
NLOT
CLA
EP
LA
BLA
BMA
PA

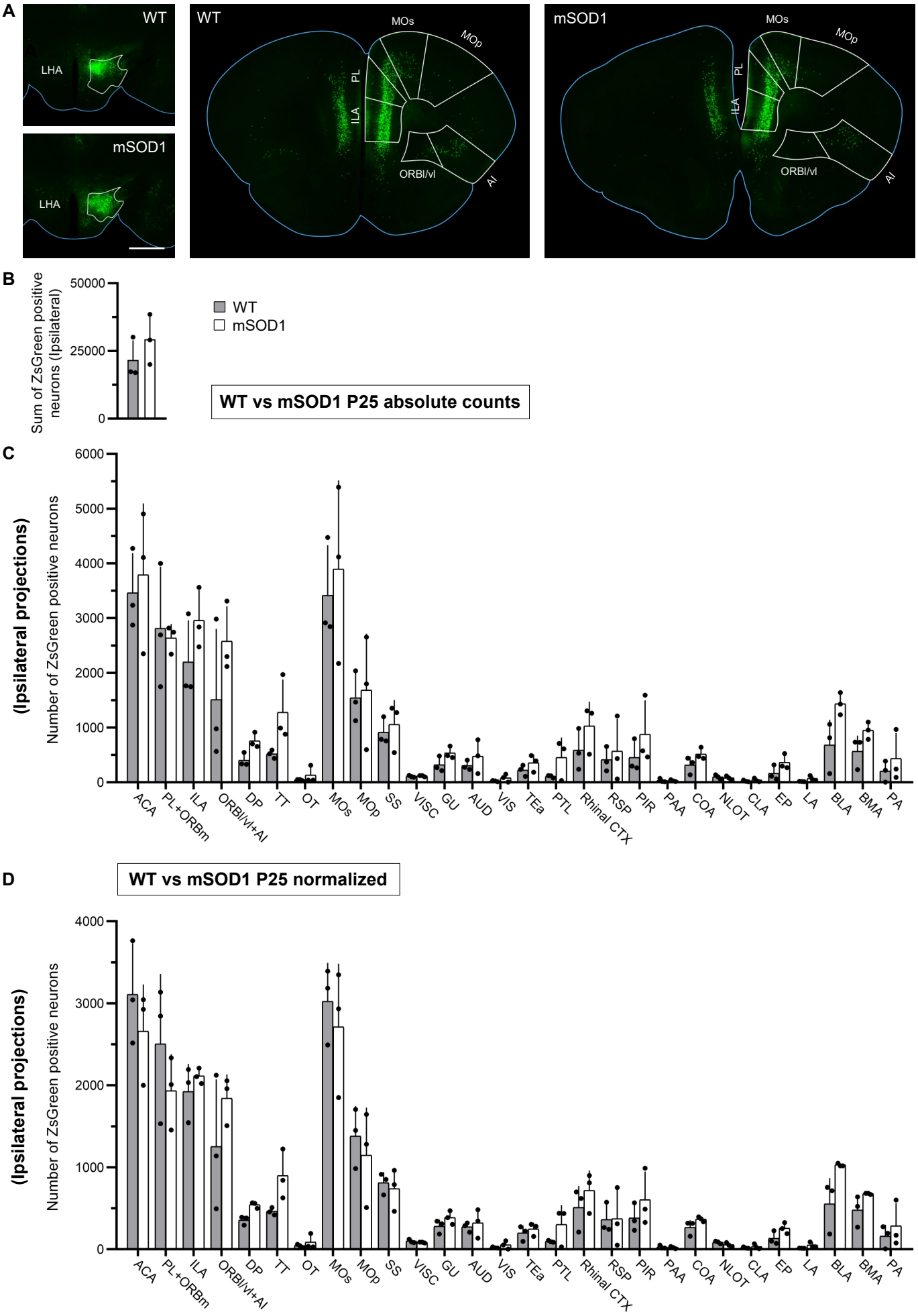
A
WT
LHA
mSOD1
LHA
WT
MOs
MOp
PL
ILA
ORBl/vl
AI
mSOD1
MOs
MOp
PL
ILA
ORBl/vl
AI
B
Sum of ZsGreen positive neurons (Ipsilateral)
50000
25000
0
WT
mSOD1
WT vs mSOD1 P25 absolute counts
C
(Ipsilateral projections)
Number of ZsGreen positive neurons
6000
5000
4000
3000
2000
1000
0
ACA
PL+ORBm
ILA
ORBl/vl+AI
DP
TT
OT
MOs
MOp
SS
VISC
GU
AUD
VIS
TEa
PTL
Rhinal CTX
RSP
PIR
PAA
COA
NLOT
CLA
EP
LA
BLA
BMA
PA
D
WT vs mSOD1 P25 normalized
(Ipsilateral projections)
Number of ZsGreen positive neurons
4000
3000
2000
1000
0
ACA
PL+ORBm
ILA
ORBl/vl+AI
DP
TT
OT
MOs
MOp
SS
VISC
GU
AUD
VIS
TEa
PTL
Rhinal CTX
RSP
PIR
PAA
COA
NLOT
CLA
EP
LA
BLA
BMA
PA

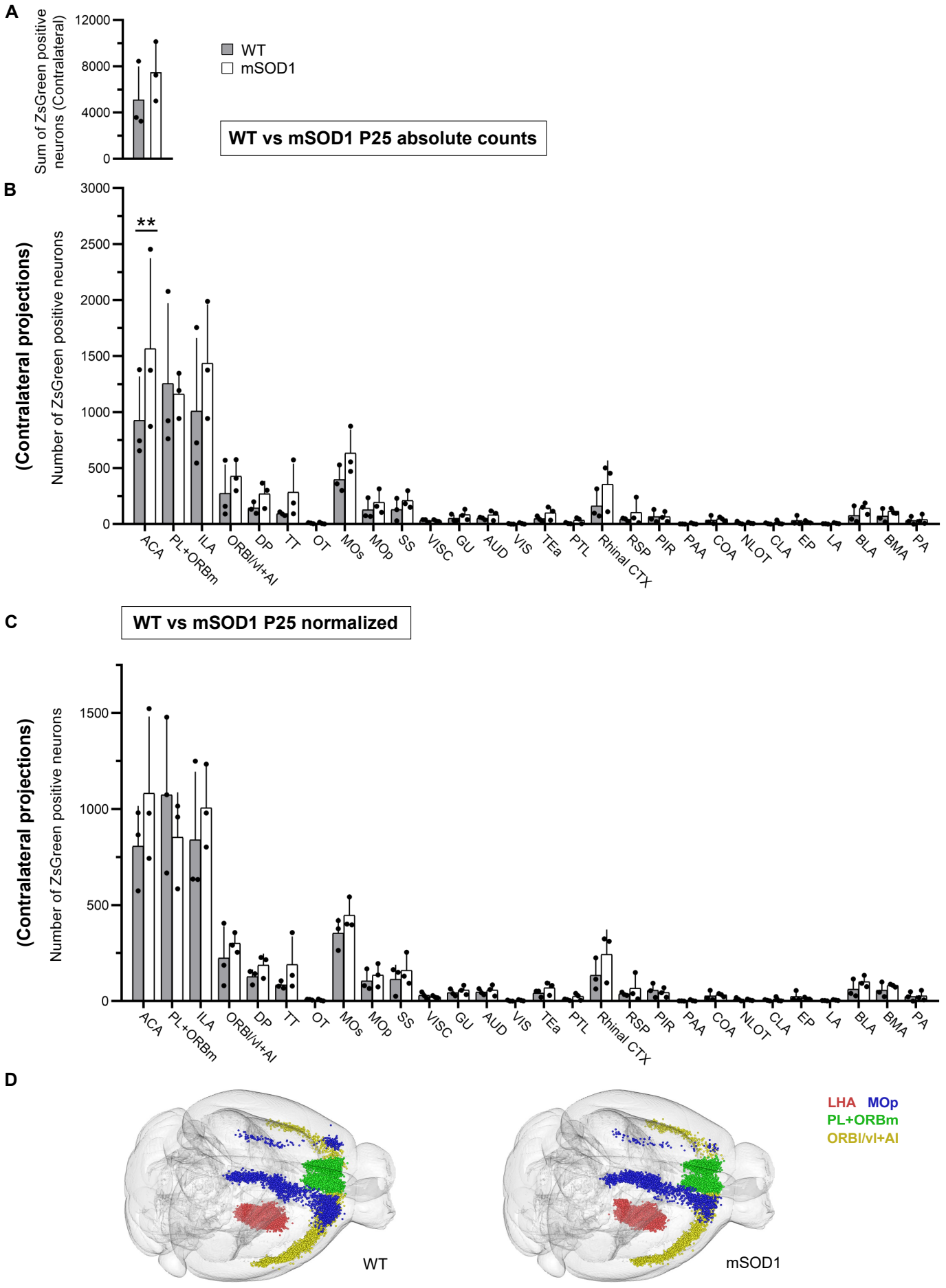
A
Sum of ZsGreen positive neurons (Contralateral)
12000
8000
4000
0
WT
mSOD1
WT vs mSOD1 P25 absolute counts
B
(Contralateral projections)
Number of ZsGreen positive neurons
3000
2500
2000
1500
1000
500
0
**
ACA
PL+ORBm
ILA
ORBl/vl+Al
DP
TT
OT
MOs
MOp
SS
VISC
GU
AUD
VIS
TEa
PTL
Rhinal CTX
RSP
PIR
PAA
COA
NLOT
CLA
EP
LA
BLA
BMA
PA
C
WT vs mSOD1 P25 normalized
(Contralateral projections)
Number of ZsGreen positive neurons
1500
1000
500
0
ACA
PL+ORBm
ILA
ORBl/vl+Al
DP
TT
OT
MOs
MOp
SS
VISC
GU
AUD
VIS
TEa
PTL
Rhinal CTX
RSP
PIR
PAA
COA
NLOT
CLA
EP
LA
BLA
BMA
PA
D
LHA
MOp
PL+ORBm
ORBl/vl+Al
WT
mSOD1

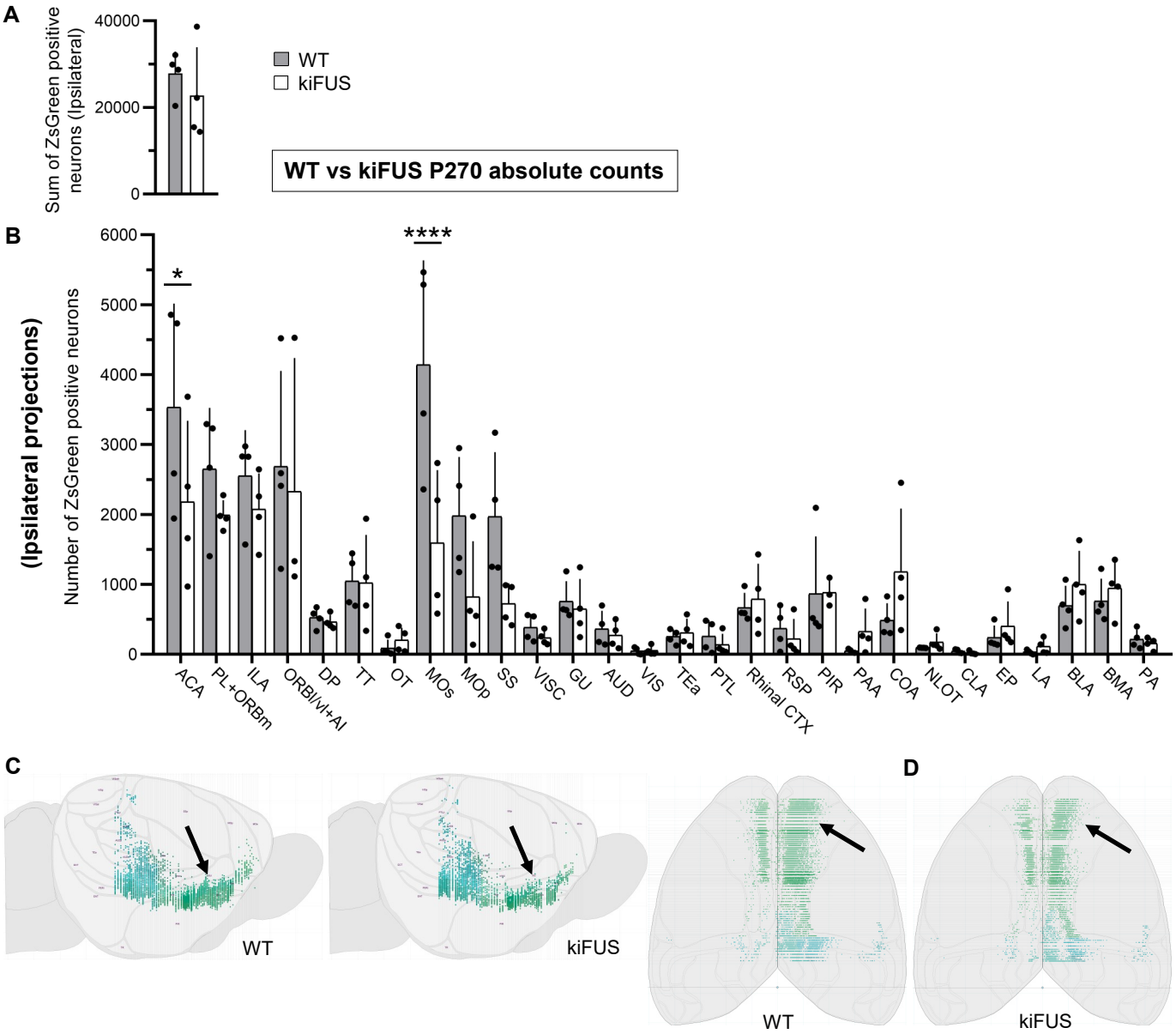
A
Sum of ZsGreen positive neurons (Ipsilateral)
40000
20000
0
WT
kiFUS
WT vs kiFUS P270 absolute counts
B
(Ipsilateral projections)
Number of ZsGreen positive neurons
6000
5000
4000
3000
2000
1000
0
*
****
ACA
PL+ORBm
ILA
ORBl/vl+AI
DP
TT
OT
MOs
MOp
SS
VISC
GU
AUD
VIS
TEa
PTL
Rhinal CTX
RSP
PIR
PAA
COA
NLOT
CLA
EP
LA
BLA
BMA
PA
C
WT
kiFUS
D
WT
kiFUS

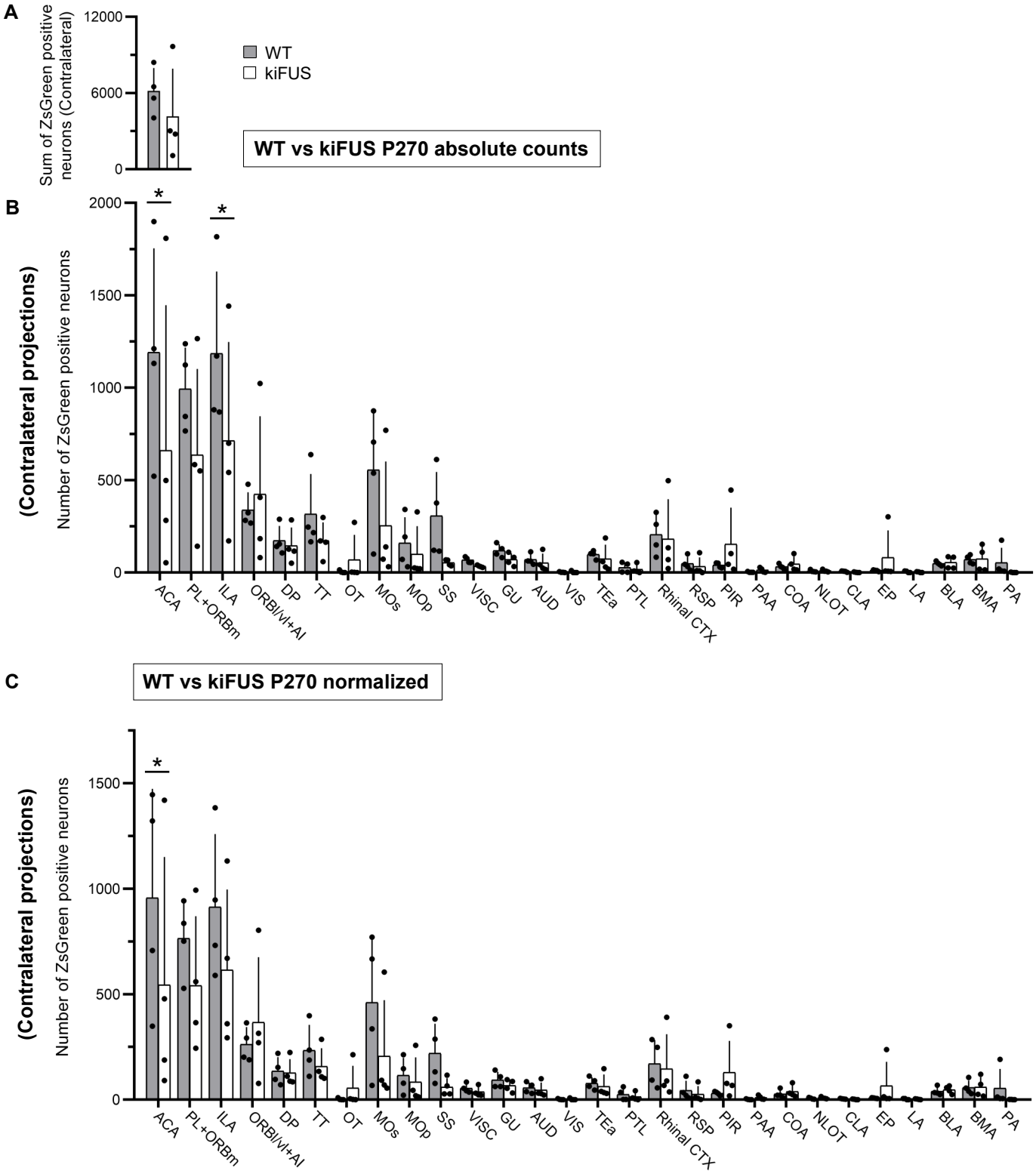
A
Sum of ZsGreen positive neurons (Contralateral)
12000
6000
0
WT
kiFUS
WT vs kiFUS P270 absolute counts
B
(Contralateral projections)
Number of ZsGreen positive neurons
2000
1500
1000
500
0
*
*
ACA
PL+ORBm
ILA
ORBl/vl+AI
DP
TT
OT
MOs
MOp
SS
VISC
GU
AUD
VIS
TEa
PTL
Rhinal CTX
RSP
PIR
PAA
COA
NLOT
CLA
EP
LA
BLA
BMA
PA
C
WT vs kiFUS P270 normalized
(Contralateral projections)
Number of ZsGreen positive neurons
1500
1000
500
0
*
ACA
PL+ORBm
ILA
ORBl/vl+AI
DP
TT
OT
MOs
MOp
SS
VISC
GU
AUD
VIS
TEa
PTL
Rhinal CTX
RSP
PIR
PAA
COA
NLOT
CLA
EP
LA
BLA
BMA
PA